A Non-Extensive Statistical Physics view to the temporal properties of the recent aftershock sequences of strong earthquakes in Greece

Sophia-Aikaterini Avgerinou[1], Georgios Michas[1,2] and Filippos Vallianatos [1,2]

1 Section of Geophysics – Geothermics, Department of Geology and Geoenvironment, National and Kapodistrian University of Athens, 15784 Panepistimiopolis, Athens, Greece.

2 Institute of Physics of Earth's Interior and Geohazards, UNESCO Chair on Solid Earth Physics and Geohazards Risk Reduction, Hellenic Mediterranean University Research Center, Grete, Greece.

July, 2021

Table of Contents

Abstract

Greece represents one of the most seismically active regions in Europe. Over the last five years seismic activity in Greece presents a series of strong earthquakes, with magnitudes that reach up to M_w=7.0. Our analysis is focused on the recent strong events, as that of the M_w6.0 Elassona (03/03/2021), the M_w5.1 Parnitha (19/07/2019), the M_w6.6 Zakynthos (25/10/2018), the M_w6.6 Kos (20/07/2017) and the M_w6.1 Mytilene (12/06/2017) earthquakes. In this work we study the temporal evolution of the aftershock sequences that were triggered by the mainshocks, based on the probability distributions of interevent times between the successive events. We approximate the observed distributions with a statistical mechanics model derived in the framework of Non-Extensive Statistical Physics (NESP). NESP provides an essential generalization of the Boltzmann-Gibbs statistical mechanics for complex systems in which memory effects, (multi)fractal geometries and long-range interactions, among other properties, are important. We show the applicability of NESP in the temporal evolution of the recent aftershock sequences in Greece and demonstrate the existence of a crossover behavior from power-law ($q\neq1$) to exponential (q=1) scaling for greater interevent times. We further discuss the observed crossover behavior in terms of superstatistics.

Introduction
Seismic sequence is called the set of earthquakes that are born in a place during a relatively short period of time, usually in the order of a few weeks, during which, the frequency of earthquakes in that place is significantly increased. In most cases, an earthquake is distinguished from the other earthquakes in the sequence, because its magnitude is much larger than the size of any other earthquake. This earthquake is called the mainshock. The earthquakes of the sequence that follow the main event are called aftershocks. Aftershock sequences are generally considered as a significant part of the earthquake occurrences, because a strong mainshock can produce a large number of aftershocks in a short time and in a small region. Many aftershocks are located in and around fault rupture regions after a mainshock. Most earthquakes are due to the movements of the lithospheric plates, and as a result the zones of intense seismic action are essentially identical to the edge of the plates. Greece is located at the limits of contact and convergence of the Eurasian plate with the African, which explains the intense seismicity. The seismicity of a place is determined by the frequency of the occurrence of earthquakes and their magnitudes. According to statistics, Greece, in terms of seismicity, ranks first in the Mediterranean and Europe as well as sixth place in the world.

Based on data of the last four years we observe that Greece is characterized by earthquakes with magnitudes that reach up to Mw=7.0. In this work, we present a seismotectonic study of the 2017-2021 seismic events of the Hellenic Area and investigate the aftershock sequence for each earthquake separately. More specifically, we study the aftershock sequence with particular emphasis on the interevent times as well as the distribution of them.

Geological and seismotectonic setting

Greece is the most geologically active region in Europe, due to its special place in the global system of lithospheric plates. More specifically, Greece is located at the southeastern end of Europe, an area that has witnessed significant geological processes, such as the Alpine orogeny. This orogenic phase led to the uplift of major mountain ranges (e.g. the Dinaric Alps and the Pindus range) and was the driving force behind the formation of complex tectonic structures. This activity is still present in the region and is expressed through intense deformation and high seismicity, concentrated in areas such as the Hellenic Arc (Kapetanidis V. et al., 2020).
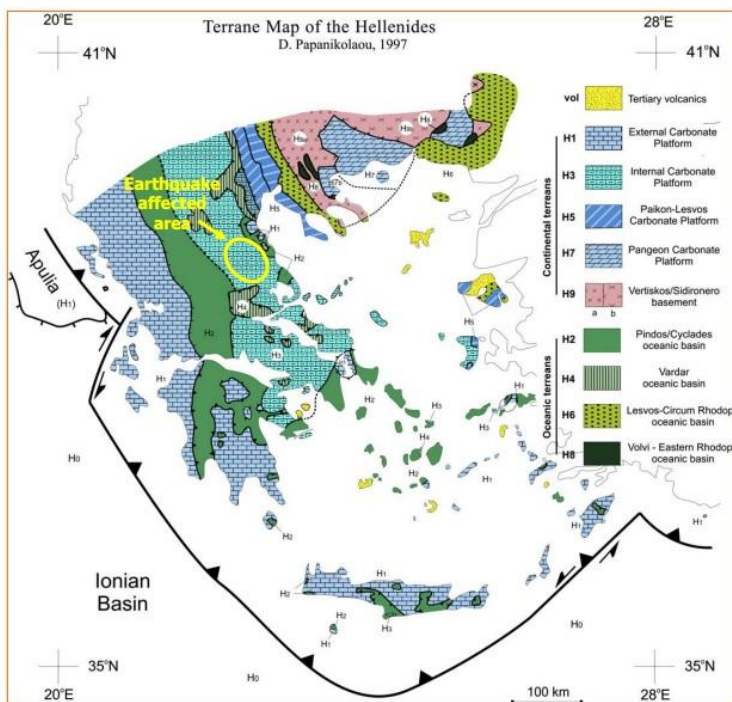
1. Elassona

Figure 1: The geology of Greece according to Papanikolaou (1997). The earthquake-affected area comprises geological formations belonging to the tectonostratigraphic terrane H3 of the Internal Carbonate Platform. (Lekkas E. et al., 2021).

The Thessaly Basin is located at the backarc area of the Aegean microplate and is one of the most seismic active areas in Greece with earthquakes with magnitudes ranging from 6.0 to 7.0. It's seismicity is related to two fault zones in the Thessaly Basin. The northern one is associated with earthquakes with magnitudes up to 6.5 and the southern one, which is associated with magnitude up to 7.0.

About The Thessaly plain is particularly interesting from both the neotectonic and active tectonics point of view, because it is a well-defined, inland basin, filled with recent Quaternary and Neogene sediments. The basin is surrounded by mountainous areas, with an average altitude exceeding 1000m. More specific, Antichassia and Kato Olympos mountains occupy the northern part of Thessaly area, Ossa, Mavrovouni and Pelion Mountains dominate its eastern section, while

the western and southern parts of the basin are characterized by the Pindos and Othrys ranges, respectively. In the middle of the Thessaly plain a morphological ridge exists, which consists of the mountains of Zarkos and Titanos. The axis of this ridge divides the plain into an eastern and a western basin.

Figure 2: The two fault zones: the northern fault zone, which is associated with earthquakes with magnitudes up to 6.5 and the southern fault zone associated with earthquakes with magnitude up to 7.0 (Lekkas E. et al., 2021).

Moreover, The Thessaly plain covers part of the Pelagonian and Subpelagonian geological zones. This area is characterized by strong stratigraphic complexity and tectonic deformation, of both the alpine and the post-alpine period. Specifically, the geological formations include alpine, molassic and post-alpine formations. The basement and the margins of the affected area is mainly composed of gneisses of Paleozoic age, and of Neopaleozoic – Lower-Middle Triassic formations including gneiss schists, gneisses, schists with orthogneiss and marble intercalations at their lower members and schists at the upper members of the Neopaleozoic – Lower-Middle Triassic formations. As regard the post-alpine deposits, the Holocene is represented by recent deposits in the river and torrent beds and terraces, alluvial deposits within the affected flood plains of Titarissios and Pineios Rivers and recent scree in slopes. Pleistocene talus cones, scree, fluvial-terrestrial and fluvial-lacustrine deposits are also part of the post-alpine deposits. Neogene marls and clays occur in the earthquake affected area (Lekkas E. et al., 2021).

2. Parnitha

The Athens basement belongs to alpine formations outcropping in the mountains and the hills of the region (Foumelis M., 2019). The area is characterized by a complex post-alpine morphotectonic structure, formed by the tectonic horsts of the Parnitha, Aegaleo, Hymettus and Penteli mountains and the tectonic grabens of the Thriassio plain and that of the western Athens basin. Their main directions are EW and NE-SW (Kapetanidis V. et al., 2020). Neogene sediments and quaternary terrestrial deposits overlie unconformably the basement formations.

According to seismic and gravity geophysical surveys, the thickness of the post-alpine sediments show considerable spatial variability, which seems directly related to the presence of buried fault structures. At the northern part of the basin the major thickness of post-alpine sediments exceeds 600 m showing a decreasing trend towards the SW, whereas 450 m are reported within the central part of the Thriassio Basin. The broader area is controlled by two main sets of fault zones trending NNE–SSW to NE–SW at the eastern part and WNW–ESE to E–W structures prevailing in the western part, forming a multi-fractured pattern of blocks with different kinematic characteristics and independent evolution. This also reflects the level of their neotectonic activity, with WNW–ESE to E–W trending faults considered relatively more active than those of NW–SE. Many of these fault zones have a pronounced influence on the topographic relief of the region, which is visible in aerial photographs and satellite imagery. Measurements on scarp morphometry and kinematics and displacement of Pleistocene terraces characterized several fault segments, mainly over Parnitha Mt., as active. The majority of these findings refer to the relatively more active part of Attica (Foumelis M., 2019).
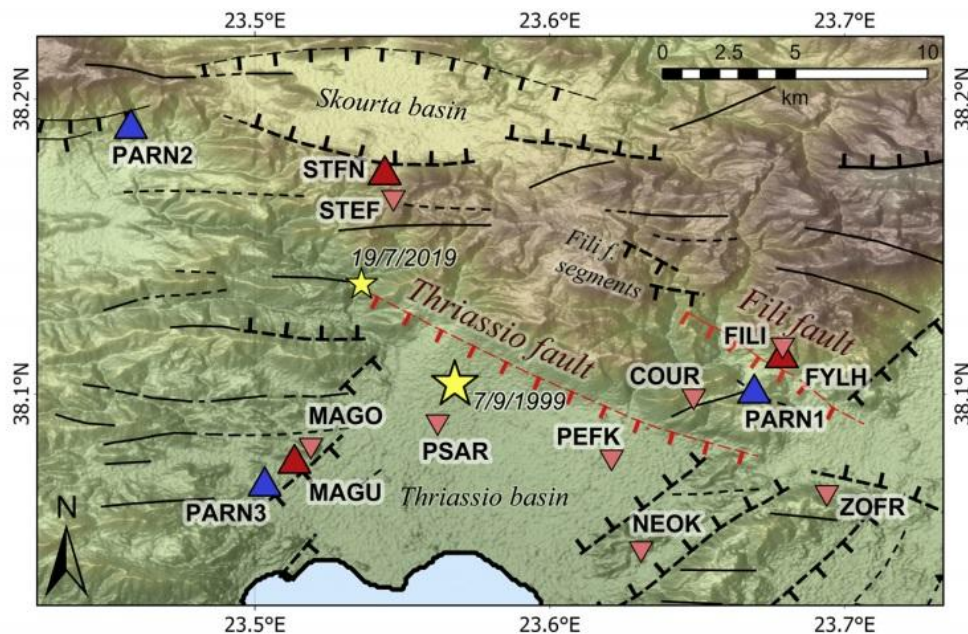

Figure 3: Study area, indicating the locations of the local seismological stations that were installed to record 2019 aftershocks (triangles; red: SL-NKUA, blue: GI-NOA). Solid and dashed fault lines denote certain/uncertain or buried faults, respectively, with ticks marking the dip-direction, where available. The two important candidate faults of Thriassio and Fili are drawn with red colour. Fault traces are composed after Lekkas (2001); Foumelis (2019); Goldsworthy et al. (2002); Stefatos et al. (2002); Karakonstantis and Papadimitriou (2010) and the NOA faults database (Ganas et al., 2017), (Kapetanidis V. et al., 2020).

Especially, the epicentral region of the earthquake of 2019 is located along the southeast facing slopes of Mt. Parnitha. The mountain block is made of Triassic–Cretaceous limestones that overlie Palaeozoic– Triassic shales and sandstones alternating with phyllites and quartz conglomerates. The prevailing tectonic structures within these rocks include EW- and NW-trending thrusts. Two SW-dipping normal faults dominate the neotectonic structure of this region: a N120°E striking fault referred to as Aspropyrgos fault and a N130°E fault referred to as Fili fault. The Aspropyrgos fault is expressed as a prominent scarp

that extends for 12 km and separates the limestone basement (to the north) and the plain deposits (to the south) where Athens is situated. Parallel to this fault and at 2 km and 4 km to the north, two other faults can be identified from the geological maps and satellite images. No coseismic displacement due to the Athens earthquake was found on the listed faults (Tselentis G.-A. and Zahradnik J., 2000). In conclusion, it is worth considering that the spatial distribution of the 2019 aftershocks sequence is certainly less widespread, mainly confined to the same area as the western half of the 1999 aftershocks zone (Kapetanidis V. et al., 2020).

3. Zakynthos

The southern Ionian Islands (Lefkada, Ithaca, Kefallonia, and Zakynthos) because of their position lie close to the western edge of a tectonic plate, earthquakes are common. All the islands are dominated by limestone (210-36 million years old), which has been cut by many faults during compression of the region (Michael Denis Higgins, 2009). Zakynthos is a seismically active area, and a part of the Apulian foreland of the Hellenide Orogen which is built up due to the progressive collision of Eurasian and African major tectonic plates that form the Earth's uppermost layer.
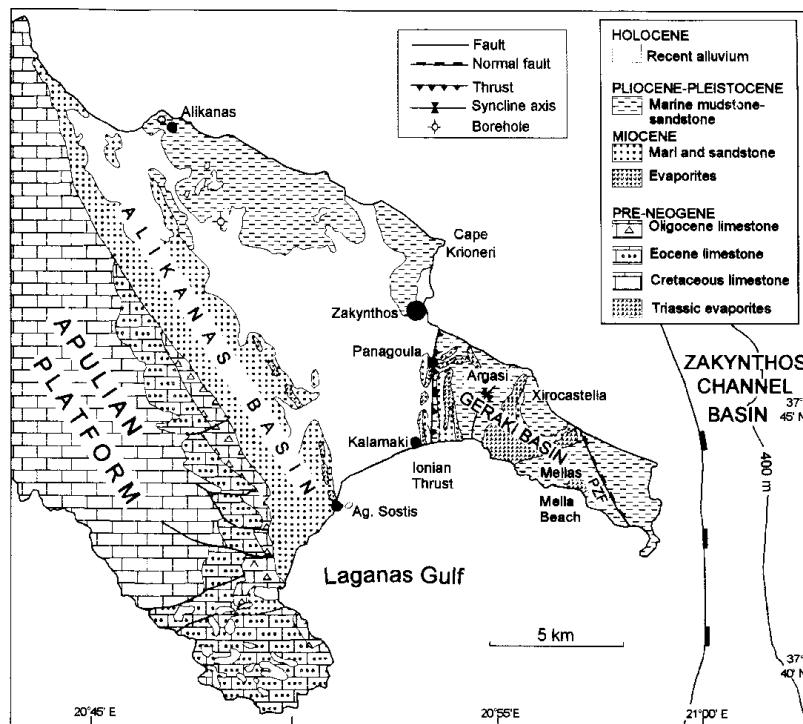

Figure 4: Geological map of south-eastern Zakynthos island (modified from Underhill, 1988; Dermitzakis et al., 1979), PZF=Porto Zorou Fault, (Zelilidis A. et al., 1998).

From the point of view of geology, the island is divided into the western part which is with lies in the Pre-Apulian Zone and the eastern part lies in the Ionian Zone, the most western zones of Greece. These two zones are divided by the Ionian thrust fault. The Ionian zone is considered to be overthrusted to the Paxos zone. The Paxos zone consists of an east-dipping Upper Cretaceous to Plio-Quaternary sedimentary succession. The main part of the Paxos zone in the island, which consists of Upper Cretaceous limestones that are overlain by Eocene limestones (Kati M., 1999). Limestones cover more than 50% of the total area of the island (see Vraxionas Mountain). Further to the East, a narrow Oligocene zone overlies on the Eocene deposits and consists of marly

limestones and marls. There maining part is covered by Miocene and Pliocene. In the lower Miocene beds, occur gypsum deposits. The Pliocene sequence contains two units: (a) a lower of marls and marly sandstones, and (b) an upper of sandstones deposits within marls (Kypseli unit).

One the other hand, the Ionian zone deposits consist of Triassic gypsum and evaporites, which are strongly affected by diapirism and black limestones that overlay the gypsum beds. The remaining part of the Ionian zone is covered by Pliocene sediments (marl sand sandstones). Exposed diapirs are dominated by gypsum. The Quaternary deposits include Pleistocene and Holocene deposits, which are developed in the eastern part of the island and consist of alternating beds of gravels, sands, clays and silty clays. The Pleistocene deposits cover the hills and the alluvial deposits the low-lands, with an average thickness of 5–10 m. Contractional structures characterize many areas in the Cretaceous out-crop and also include the development of numerous NW-SE oriented reverse faults discharged through submarine springs in the Ionian Sea. Groundwater flow is controlled by the pattern of the existing fracture system (Diamantopoulou P., Voudouris K., 2008).

4. Kos

The island of Kos off the Turkish coast in the Eastern Aegean Sea forms part of the Hellenic–Tauric system, a complex mountain belt extending from south Eastern Europe to Turkey. The Hellenic arc results from the collision of the Apulian microcontinent with the crystalline complexes of northeastern Greece in Mesozoic to Cenozoic times. It displays a pronounced southwest vergent nappe character. Apart from minor Palaeozoic units, the nappes consist of Mesozoic to Cenozoic sediments and magmatic rocks, including ophiolites. Some of these nappes have been subject to different degrees of metamorphism during collision. Metamorphism and thrusting took place during several events between Jurassic and Miocene times.

The geological units on the island of Kos form part of the Central Hellenic nappes. The oldest units form the Dicheo Massif in the central part of the island towards the south coast. They consist of Permocarboniferous marls, impure limestones and sandstones, phyllites and rare mafic intercalations that have been subject to post-Permocarboniferous regional metamorphism at very low grades. At 12 Ma, this series was partly metamorphosed by the intrusion of a large quartz monzonite. Subsequent to intrusion and exhumation Permocarboniferous metasediments and Miocene quartz monzonite were tectonically overridden by Cretaceous to Eocene limestones that crop out mainly north and west of the pluton. After tectonic emplacement of these limestones, the area west of the Dicheo Massif was covered by Pliocene and Pleistocene sediments and mostly Quaternary volcanics. To the east, the Dicheo Massif is tectonically bordered by a flysch sequence of late Cretaceous to Tertiary age. The Permocarboniferous sedimentary unit contains a basal marble–metapelite sequence (1000 m), followed by 200 m of massive marble, 100 m of calc-silicate rocks and a top layer of dolomite marble. The unit is mainly exposed to the east of the quartz monzonite intrusion. Within the basal marble–metapelite sequence and the calc-

silicate rocks, contact metamorphic mineral assemblages and mineral isograds have been described and mapped. From mineral paragenesis and experimentally determined phase relations, temperatures of ≈800°C at the contact declining to ≈500°C over a distance of 4 km at pressures of 0,3–0,6 GPa were deduced (Kalt A. et al., 1998).
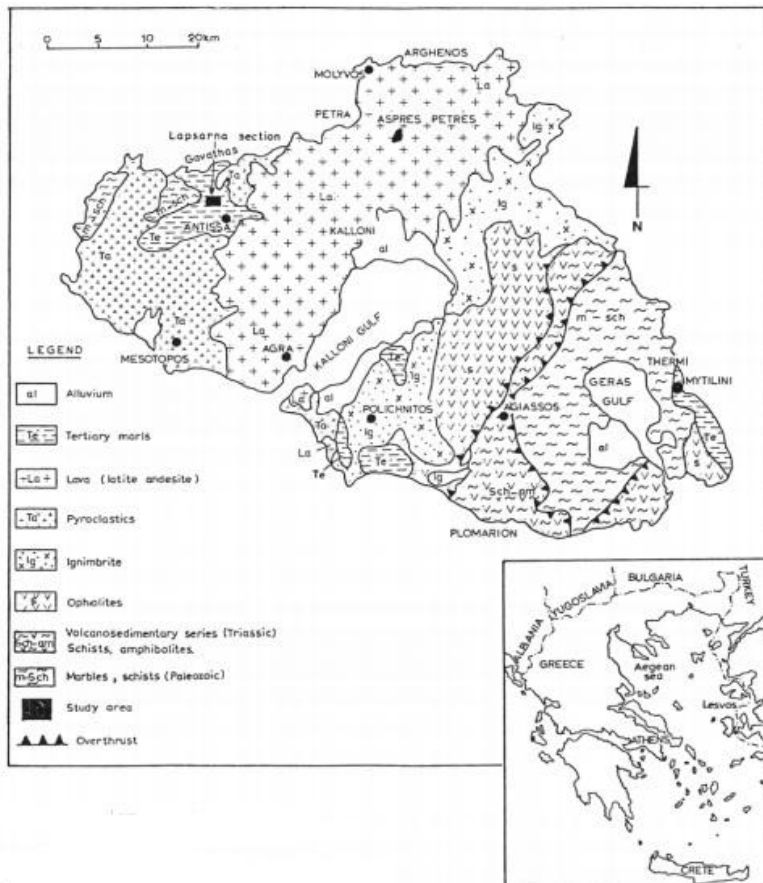
5. Mytilene

Figure 5: Geological Map of Lesvos, Mytilene (Kelepertsis A., 1992).

Lesvos is the third largest island in Greece and is located in the NE part of the Aegean Sea, very close to the Asia Minor coast. Specifically, it is located in the SW of the gulf of Adramyt, opposite Aivali, in an important alcove presented by the Asia Minor coastline, which is set in its northern part by the Adramytion fault.

This rift is an important tectonic element of the wider region. It is a clockwise horizontal displacement fault with a WNW-ESW address, which is part of the rifts alongside the great rift of North Anatolia and its conclusion in the Aegean Sea.

Mytilene is characterized, in its southern part, by two large enclosed bays, by the bay of Kalloni and the bay of Gera, which are related to the tectonic evolution of the wider area of the North Aegean and especially to the neotectonic action that resulted in the sinking of Aegida.

It is well known that Lesvos has a strong neo-tectonic action because it is from a geotectonic point of view in a position with strong modern mobility, as the micro-plate of Turkey moves towards to SW and pushes the space of the Aegean Sea, forcing it to make an expansion in the same direction. The wider tectonic field in the NE Aegean region is dominated by the action of large clockwise horizontal displacement fractures, on which the movement of the area is mainly made and which form, together with normal motion shallow surfaces, the Asia Minor coastline (Thomaidou E. L., 2009).

As regards to the geology of the island, Lesvos from base to top consists from the following units (Stamatakis M., et al.):

a. The autochthonous unit which includes:
   1. the neopaleozoic formations
   2. the triassic formations
b. The allochthonous units which include:
   1. the tectonic nappe of the volcanosedimentary formations
   2. the unit of the tectonic nappe of the ophiolitic rocks
c. The unit of postalpine formations.

Autochthonous unit

This unit is a series of formations from the Neopaleozoic until the Upper Triassic without Stratigraphie uncorformities and it consists entirely of metaclastic rocks with lenses and intercalations of crystalline limestones and dolomites. It is characterized by a very low-grade metamorphism and by the absence of rocks of igneous origin.

The Neopaleozoic formations are extended on the southeast part of the island, where the visible thickness, in places, is more than 1 km. In the northwest part of the Island they have relatively small extensions (areas of Sigri, Gavathas, Eressos) and they are found under the post-alpine volcanic and lacustrine formations of this area.

They consist of schists (mainly micaceous, sericitic and chloritic) alternating with metasandstones (mainly arkoses), quartzites and crystalline carbonate rocks in the form of lenses and intercalations. Generally the extension and the thickness of the carbonate rocks are always limited, except in the upper parts of certain areas, where the carbonates dominate. In these rocks and in several localities and different Stratigraphie horizons, a rich fauna was found consisting of foraminifers, algae, lamellinbranchs, gastropods, echinoderms, crinoids and corals, of Carboniferous-Permian age. The Triassic formations represent the upward normal transition of the Neopaleozoic formations and they are found only in the southeast part of Lesvos. They consist mainly of schists and metasandstones. Within these formations usually occur very thick intercalations of crystalline carbonates, where Megalodon have been found by Katsikatsos.

Characteristic of these formations is the presence of breccia and big carbonate blocks, mainly within the upper horizons of these formations (Stamatakis M., et al.).

Allochthonous units

Those units overthrust above the autochthonous formations and they are divided into two tectonic nappes:

a. the lower comprising Triassic volcanosedimentary formations and
b. the upper comprising ophiolitic rocks.

The nappe of the Triassic volcanosedimentary formations occupies a large area in the southeast part of the island and its thickness exceeds, in places, the 1 km. It consists of various types of metabasites, which usually dominate in the upper

parts, and metasediments represented mainly by crystalline limestones and dolomites and secondarily by schists of various mineralogical composition (chlorite, mica, sericite, e.t.c.) and conalomerates. The crystalline limestones and dolomites appear in the form of lenses and intercalations of various thicknesses (from a few up to several hundred meters). The age of these formations has been determined by the characteristic fossils of Lower-Middle Triassic, found in the carbonate rocks of these formations (Katsikatsos et al., 1982). The rocks of the volcanosedimentary formations have suffered initially a low-grade metamorphism in the pumpellyite-actinolite-chlorite zone. Characteristic of these formations is the presence, in places, of glaucophane, providing a higher pressure during their period of metamorphism. The ophiolitic nappe occupies a large area in the southeast part of Lesvos and towards the nothwest they are covered by the volcanic formations of the island. The ophiolitic rocks are found overthrust, in their larger part, on the volcanosedimentary formations and they are divided into two parts which are in tectonic relation:

a. The upper part which mainly consists of ultramafic rocks and

b. The lower part consists of metamorphic basic ophiolitic rocks.

The upper part consists entirely of ultramafic rocks, of various degrees of serpentinization. Veins of pyroxenites and gabbros intersect these ultramafic rocks, in places. The thickness of the upper part exceeds in places the 1000 m. The lower part appears in several places, always intercalated tectonically between the upper part of the ophiolitic rocks and the underlying volcanosedimentary formations. The thickness of the lower part of the formations reaches, in places the 300 m and they are mainly amphibolites and amphibolitic schists, originating from mafic ophiolitic rocks. The rocks of the two groups of the ophiolitic tectonic nappe have suffered at least one very low grade metamorphism in the pumpellyite-actinolitechlorite zone, similar to the one that they have suffered the formations of the volcanosedimentary nappe (Stamatakis M., et al.).

The unit of post-alpine formations

The post-alpine formations are extended in large areas of the island and mainly volcanites and Neogene formations of lacustrine facies, as well as Tertiary deposits represent them (Stamatakis M., et al.).

Applied Methodology

Seismological methods are the means by which the nature and origin of Seismic Events are determined. The main elements used in this determination are detection, recording interpretation, and analysis. Through the application of seismological methods, we can be informed about the structure of the earth, the causes of earthquakes, and how we may in the future predict the location, the magnitude and time of occurrence of earthquakes. Focusing more in aftershocks sequences, statistical characteristics can give valuable information about the fault structure, cracks distribution, and earthquake migration. There are many

ways to describe the aftershock activity from a mainshock, aftershock characteristics can be described, as we'll see, in time (modified Omori law, Utsu et al., 1995) and magnitude (Gutenberg-Richter law, Gutenberg and Richter, 1944).

1. Gutenberg–Richter law *(G-R law, b-value)*

In Geology there is a seismic law which states that there is a constant empirical relationship between the frequency of earthquakes in a region and their magnitudes. More specifically, Gutenberg and Richter (1944) relation describes the cumulative earthquake-size distribution. The relationship between the frequency of occurrence and magnitude of aftershocks can be given with the following empirical equation:

$$\log_{10} N(M) = a_t - b M \quad (1)$$

where,
N(M): is the cumulative number of aftershocks with magnitudes equal to or greater than M,
a_t and b values: are positive constants.

a_t-value describes the earthquake activity level and shows significant changes from region to region because it depends on observation period and investigation area. In addition, the constant a_t depends on the seismicity of the area, the area of the surface covering by the epicenters and the length of time covered by the list. Parameter b (b-value) depends on the stress and mechanical properties-homogeneity of the material in the focal area (hypocenter). Moreover, it depends on the age and tectonics of the study area. The estimated b-value usually equals to 1 but varies mostly between 0.5 and 1.5 (Papazachos et al., 2005). In addition, b-value describes the magnitude distribution for a particular time interval, which can be used for estimation of seismic hazard.

Another way can be given as the Gutenberg-Richter (G-R) scaling law which describes the relationship between the frequency of occurrence and aftershock magnitudes. Thus, this power-law distribution can be applicable to aftershock magnitude-frequency analysis.

2. Modified Omori law (p-value)

This model is satisfying the temporal decay of aftershock sequences in many instances. The spatial distribution of the temporal decay of aftershocks may reflect either regional changes in the state of stress in the Earth or the material properties (e.g., Wiemer and Katsumata, 1999; Enescu and Ito, 2002; Polat et al., 2002; Bayrak and Öztürk, 2004; Öztürk et al., 2008; Nuannin et al., 2012; Arora et al., 2017).

The modified Omori law describes the amount of aftershocks that increases suddenly after a mainshock and then decreases with time. Using the following equation, the modified Omori law, examined the rate of occurrence of smaller events as a function of interevent time t of the mainshock:

$$n(t) = \frac{K}{(t+c)^p} \quad (2)$$

n(t) symbolizes the occurrence rate of aftershocks (number of aftershock per day) per unit time, t-days after the mainshock. K, p, and c values are empirically derived positive constants which depend on the total number of events in the sequence and the activity rate in the earliest part of the sequence, respectively. The total number of aftershocks is controlled by the K-value. The latter is, called aftershock productivity, a normalizing parameter that is dependent on the total amount of aftershocks and the threshold magnitude. In many cases K-value is estimated at 1 (Bruce E. Shaw, 1993).
So, the above equation converts to:

$$n(t) = \frac{1}{(t+c)^p} \quad (3)$$

c-value is widely considered as a delay between the mainshock rupture end and the start of the power law aftershock decay rate. Moreover, it depends on the rate of activity in the earliest part of the sequence. This is, also, a controversial quantity (Utsu et al., 1995) and strongly affected by incomplete detection of small aftershocks in the early stage of sequence. That specific parameter increases with the lower magnitude threshold of the considered aftershocks and has a non-zero value.
The most important parameter is the p-value which defines the mode of aftershock decay as a function of time on frequency (Öztürk S. et al., 2018). Increased p-value is used for rapid decay whereas decreased p-value means slow decay of aftershock sequences. Usually this parameter changes between 0.5 and 1.8 for various aftershock sequences, according to many researchers (Öztürk S. et al., 2018). This situation may be accompanied with the tectonic conditions of the study area such as fault heterogeneity, stress, and crustal heat flow. Lastly, we can take information about the fractal property of a pre-existing fault system in the crust but it is not clear which condition among them is more related to the p-value (Öztürk S. et al., 2018).
The modified Omori's law expresses the temporal correlation in aftershocks sequence, which as it is accepted is the pattern of a complex relaxation process that evolves after mainshock. In order to study the Omori's scaling we use the total number of aftershocks N (t) for a given time t with magnitude greater than M, as obtained integrated R (t, M), with the result (Vallianatos F. et al., 2021):

$$N(t) = \begin{cases} \frac{c}{\tau(p-1)}\left[1 - (1 + \frac{t}{c})^{1-p}\right], & p \neq 1 \\ \frac{c}{\tau}\ln(1 + \frac{t}{c}), & p = 1 \end{cases} \quad (4)$$

3. *Studying of interevent times in terms of Tsallis Entropy*

In this chapter, we used a generalized formulation of Boltzmann–Gibbs (BG) statistical physics mentioned as non-extensive statistical physics (NESP) (Tsallis C., 2009a, Vallianatos F. et al. 2016a, b, Chelidze et al. 2018 and references there in), to investigate the distribution of the interevent times in the aftershocks

sequence of study events. NESP is based on a generalization of the classic Boltzmann-Gibbs entropy and has the main advantage that it considers all-length scale correlations among the elements of a system, leading to an asymptotic power-law behavior. NESP has found many applications in non-linear dynamical systems including.

To begin with, we based on the generalized expression of entropy, as that of Tsallis, and it is suitable for characterizing complex systems with finite degrees of freedom, self-organized criticality and non-Markovian processes with long-range memory as that frequently appears in Geosciences (Telesca L. 2012, Tsallis C., 2009b, Vallianatos F.et al., 2016a,b, Vallianatos F. et al., 2018).

More specific, Telesca L. et al., investigate the temporal distribution of seismicity by estimating the H with time for earthquake magnitudes and interevent time series over the full and the aftershock-depleted catalogue, they found that the information entropy of the interevent intervals and magnitudes are significant parameters to quantify the degree of predictability of the interevent time and/or magnitude of a sequence of earthquakes. Also, due to the large frequency of small interevent intervals, the time variation of the interevent entropy revealed that the predictability of interevent times after the aftershocks increases, whereas the time variation of the magnitude entropy was indicative of a decrease in the predictability of the magnitudes (Rojas A.-R. et al, 2019).

Starting, we set as variable T the time interval between two consecutive aftershocks T, where p (T) dT presents the probability of finding the value of the parameter in the range [T, T+dT]. In order to understand a complex system which is in a non-equilibrium state, an entropic functional Sq was proposed by Tsallis C. and Vallianatos F. (Vallianatos F., Pavlou K., 2021). In terms of probability p (σ) of finding a fragment of area σ, the maximum Tsallis C. entropy Sq is expressed as:

$$Sq = k_B \frac{1 - \sum_i p^q(T_i)}{q-1} \quad (5)$$

In the above equation (5) as a parameter k_B is Boltzmann's constant, and the index q express the degree of non-additivity of the system, since our system violates the additivity property of classical BG entropy.

The non-extensive entropy Sq is, in a way, a classical entropic functional generalization since in the limit q→1 for the Tsallis entropy, we reach the well-known Boltzmann–Gibbs (BG) entropy (Vallianatos F. et al., 2018).

In earth sciences the cumulative distribution function is a traditionally used in terms of NESP and is given by the expression: $P(> X) = exp_q(-BX)$. Maximizing the parameter Sq using the Lagrange multipliers method leads us to:

$$p(T) = \frac{[1-(1-q)\left(\frac{T}{T_q}\right)]^{\frac{1}{1-Q}}}{Z_q} = exp_q \frac{(-T/T_q)}{Z_q} \quad (6)$$

The function q-exponential defined, when applicable 1+(1-q)X≥0 and $exp_q(x) = 0$, as $exp_q(x) = [1 + (1-q)x^{\frac{1}{1-q}}$. Also, the equation 6 is used in order to estimate the cumulative distribution function, as we said before, $P(> T) = \frac{N(>T)}{N_0}$ of the interevent times. The N (>T), is the number of the interevent times

with value greater than T and N_0 their total number of them. By using the distribution of $p(T)$ it appears that the P(>T) equals to $P(>T) = exp_Q(-\frac{T}{T^*})$ (7). The terms of this equation are broken down as follows:

$$T^* = T_q Q \text{ (8) And } q = 2 - \left(\frac{1}{Q}\right) \text{ (9)}$$

The latter expression indicates that introducing the Q-logarithm (Tsallis C., 2009a, b, Vallianatos F., 2011), that describe the distribution of interevent times the expression $\ln QP(>T) = -\frac{1}{T^*}T$ (10), is linear with slope$-\frac{1}{T^*}$ (Vallianatos F., Pavlou K., 2021).

According to the different values that the parameter q can receive, three different cases arise. More specifically, in the limit q→1 the q-exponential leads to the ordinary exponential function. The second case is if q>1 equation q-exponential equation exhibits an asymptotic power-law behavior with slope -1/ (q-1) and the last in contrast, for 0<q<1 a cut-off appears (Abe and Suzuki, 2003, 2005).

Aftershocks Sequences

In this section we represent the results based on the methodology we used. Especially we investigate the way that our earthquakes react to the above-mentioned models/laws.

1.1. The 2021 Elassona aftershock sequence

In this chapter, we will focus on the space-time-magnitude distribution of the aftershock sequence of the main event that hit near the capital city of Larissa in the Thessaly Region on March 3rd, 2021. The mainshock is located, as you can see in table 1, at the coordinates (22.218, 39.7322). The aftershock area, resulting from it, covers the region between the coordinates by longitudes 21.47°E-23.13°E, and latitudes 39.01°N-40.56°N.

Event No.	Earthquake	Date	Time (G.M.T.)	Lat. (°N)	Long. (°E)	Depth (km)	Magnitude	Type of Magnitude
1	Mytilene	12/6/2017	12:28:37	38,85	26,31	9	6,3	M_w
2	Kos	20/7/2017	22:31:10	36,9693	27,4057	7,1	6,6	M_L
3	Zakynthos	25/10/2018	22:54:50	37,3516	20,4922	13	6,6	M_w
4	Parnitha	19/7/2019	11:13:15	38,1291	23,5265	14,97	5,1	M_w
5	Elassona	3/3/2021	10:16:08	39,73	22,22	0,69	6,0	M_w

Table 1: Mainshock location parameters.

The mainshock had a magnitude M_w6.0 (from the Geophysical Laboratory of the Aristotle University of Thessaloniki [GL-AUTH]) and occurred at 10:16:08 GMT. The earthquake was felt throughout central and northern Greece and at first it was said that it is related to the fault of Tyrnavos, which had given a devastating earthquake in 1892, but later it became known that it was a new, uncharted, unknown until 2021 fault of the region. According to geological data, geophysical surveys and palaeoseismological excavations studying the

geological history of the fault, a slow activity is documented, which is characterized by vertical surface co-seismic displacements of 20-40 cm and a possible recurrence period of about 1-2.5 ka, as well as a low slip rate of 0.05-0.25 mm/year. The active deformation of the area is also well documented by recent primary geodetic data analysis (Chatzipetros et al., 2018; Lazos et al., 2020).

Elassona's earthquake was followed by aftershock activity in a 1-month time interval from March 3rd, 2021 to April 4th, 2021. Figure 6 shows the seismicity map, especially the distribution of the aftershock epicenters. Aftershock catalogue includes 676 aftershocks characterized by magnitudes 2.5≤M_w≤5.8. At this point, it is worth mentioning that the catalog's completeness magnitude is M_c=2.5. M_c-value varies systematically in space and time according to different networks and catalogues. Thus, M_c-value will be higher in the early part of the aftershock sequence and this high value may produce incorrect estimations on statistical analyses. Temporal variations of M_c-value can be estimated rapidly and safely by evaluating the goodness of fit to a power law (Öztürk S., Şahin S., 2018).
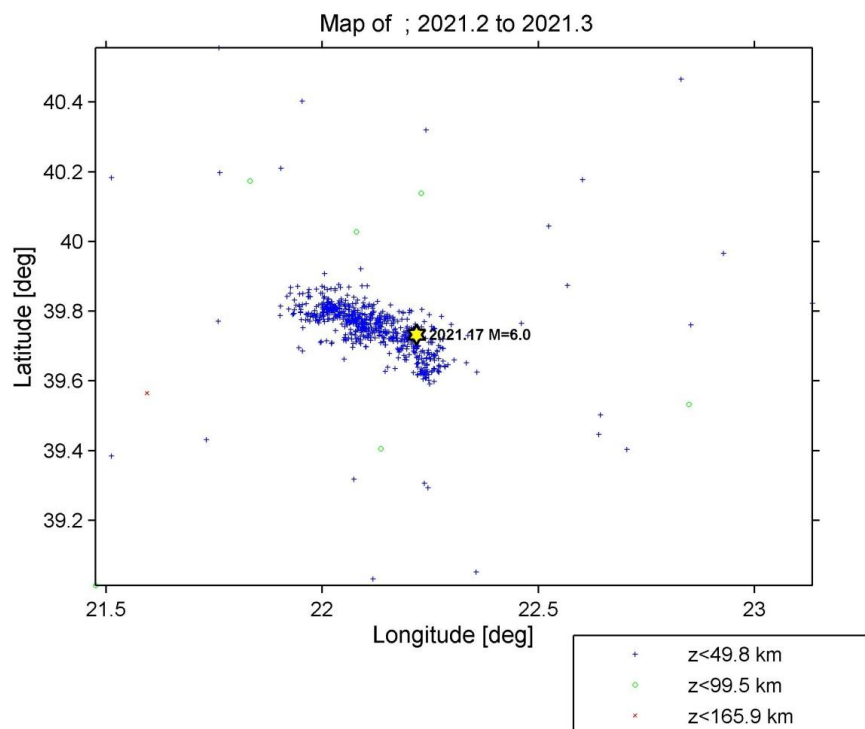
Figure 6: Epicenter distribution of the aftershock of the Elassona earthquake reported in the AUTH catalog. Different depths of the aftershocks are given by different sizes and colors. The mainshock's epicenter symbolized the yellow star (this was made by applying the Zmap software package, v.6, Wiemer, 2001).

The purpose of our work is to provide a first analysis of the scaling properties observed in the aftershock sequence. The aftershock sequence follows the Gutenberg and Richter law. The a-value and b-value came out with the completeness magnitude M_c using the maximum likelihood estimation and the best combination of maximum curvature with M_c 95% and M_c 90% probability, resulting from using the Z-map program. These two parameters

take values *b-value*=0.926±0.04 and *a-value*=5.19, respectively. However, the most important parameter is the *p-value* which defines the mode of aftershock decay as a function of time on frequency which is modified by the Omori law. In this occasion we use two different models of the law in order to cover two cases. Starting, we load all our data and run the 4 models through the Z-map. The number of events that characterize the aftershock sequence is used as data each time. In the Elassona earthquake, we refer to an aftershock sequence with 676 data, as mentioned earlier. At the end of the results, we end up with the two best models. In the first case, we select the model that displays a lower RMS value, while in the second case we attach the model that is engraved by the smallest value KS_statistics. Model 4 refers to the best RMS value, while model 3 refers to KS_statistics. Thus, each time different values of the parameters *p-value, c-value, k-value* arise depending on the model that best meets our requirements. These various values are summarized in the table 2 below.

Earthquake Elassona					
Best model (RMS)	Value RMS		Best model (AIC-KS_statistics)	Value (AIC)	Value (KS_statistics)
model 4	12,11		*model 3*	-3979,4109	0,044313
p-value	c-value	K-value	p-value	c-value	K-value
p_1=0,87	c_1=0,08	k_1=82,8	p_1=0,86	c=0,077	k_1=83
p_2=1,25	c_2=0,066	k_2=21,7	p_2=1,34		k_2=20,6

Table 2: Parameters derived from the modified Omori law.
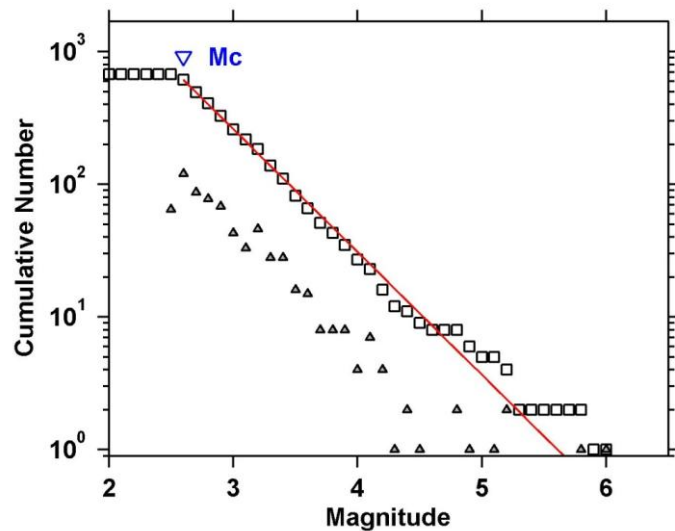
Maximum Likelihood Solution
b-value = 0.926 +/- 0.04, a value = 5.19, a value (annual) = 6.2!
Magnitude of Completeness = 2.6

Figure 7: The Guttenberg–Richter distribution for Elassona earthquake using the maximum likelihood method with the best combination of maximum curvature (Mc 95% and Mc 90% probability). The estimated values for *b-value*, *a-value* and M_c are given in Table 3.
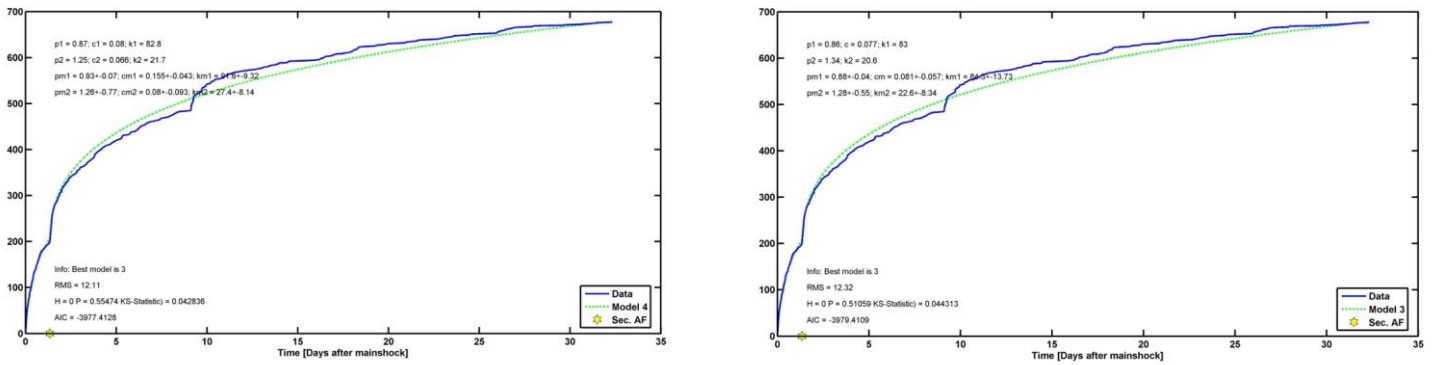
Figure 8,9: Number of aftershocks versus time (days after mainshock). The above two distributions result from the application of Omori law. More specifically, the left diagram shows the model 4 (best model RMS), while the corresponding Omori model 3 (Best model (AIC-KS_statistics) is shown on the right. The estimated values for *p-value*, *c-value*, *k-value* are given in Table 2. It is worth commenting that in a time of about 10 days after the main earthquake, there is a step in the distribution. This is because aftershock sequences themselves have a complicated hierarchical structure in which each aftershock can produce its own aftershock sequence and so forth.

Event No.	Earthquake	Mc	Time interval (t, days)	Number of aftershocks used	b-value	a-value
1	Mytilene	2.0	0,0004≤t≤10,7761	1610	0,844±0,02	4,9
2	Kos	1.6	0,00008≤t≤4,0792	6492	0,808±0,009	5,11
3	Zakynthos	2.1	0,00001≤t≤4,61954	1668	1,04±0,1	5,94
4	Parnitha	1.0	0,0004≤t≤18,0909	436	0,73±0,05	4,35
5	Elassona	2.5	0,000002≤t≤1,612170	676	0,926±0,04	5,19

Table 3: Detailed statistics for the estimation of aftershocks decay parameters.

Based, now, on the applied methodology and more specifically in paragraph 3 describing the study in terms of Tsallis Entropy, we investigate the distribution of the interevent times in the aftershocks sequence of Elassona, 2021 event. The interval time T is defined as the interval between two successful aftershocks. This approach result from the generalized expression of entropy and it is characterizing complex systems with finite degrees of freedom with long-range memory (Telesca L. 2012, Tsallis C., 2009b, Vallianatos F. et al., 2016a, b, Vallianatos F., et al. 2018).

Figure 10 illustrates the log–log plot of the cumulative distribution function (CDF), $P(> T) = \frac{N(>T)}{N_0}$ of aftershocks interevent times which has a typical Q-exponential pattern. An inspection of Fig. 10 indicates that for large values of T ($T > T_c$ where T_c is a critical interevent time) a deviation from the Q-exponential is observed. Furthermore, a fitting of Q-exponential to the observed data, up to a value close to T_c, leads to *q=1.62*, in accordance with the equations (8), (9).The obtained value q ≈ 1.67 suggests a system with one degree of freedom.
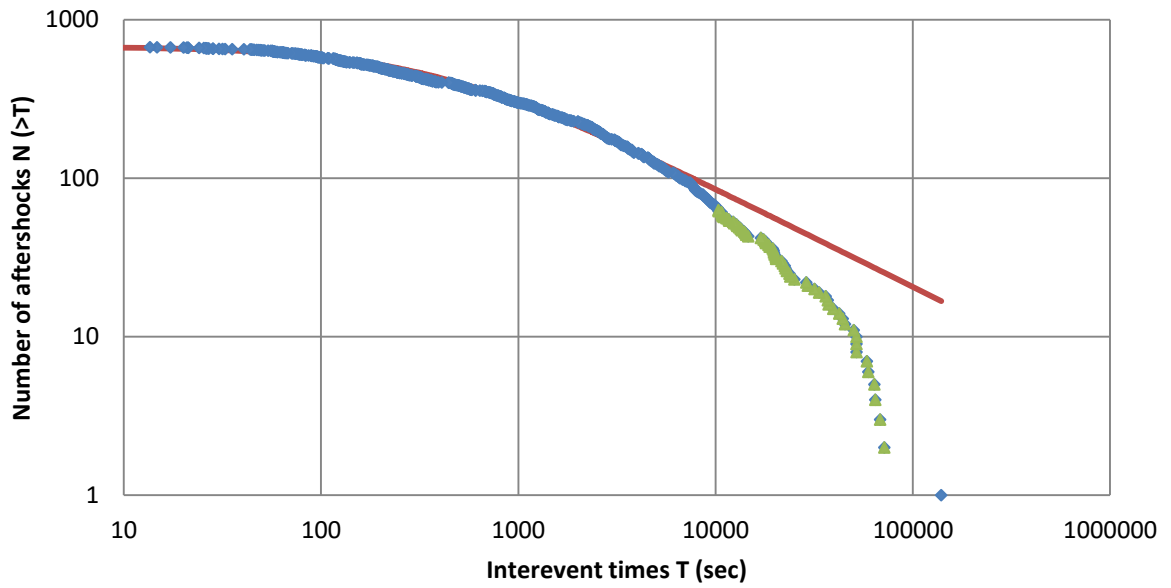
Figure 10: Interevent time distribution, $M>M_c$. The cumulative distribution functions of the interevent times for the Elassona earthquake. The red line is the q-exponential fitting with $q=1.62$.

Next, in the figure 11 we represent the $\ln_Q P(> T)$ (see equation 10) as a function of interevent time T for $q=1.62$. From the deviation from the expected linearity, the transition from one system to another we estimate that T_c has the value ≈7584 s. In this assessment we also took into consideration the correlation coefficient R_2, as shown in the figure 12.
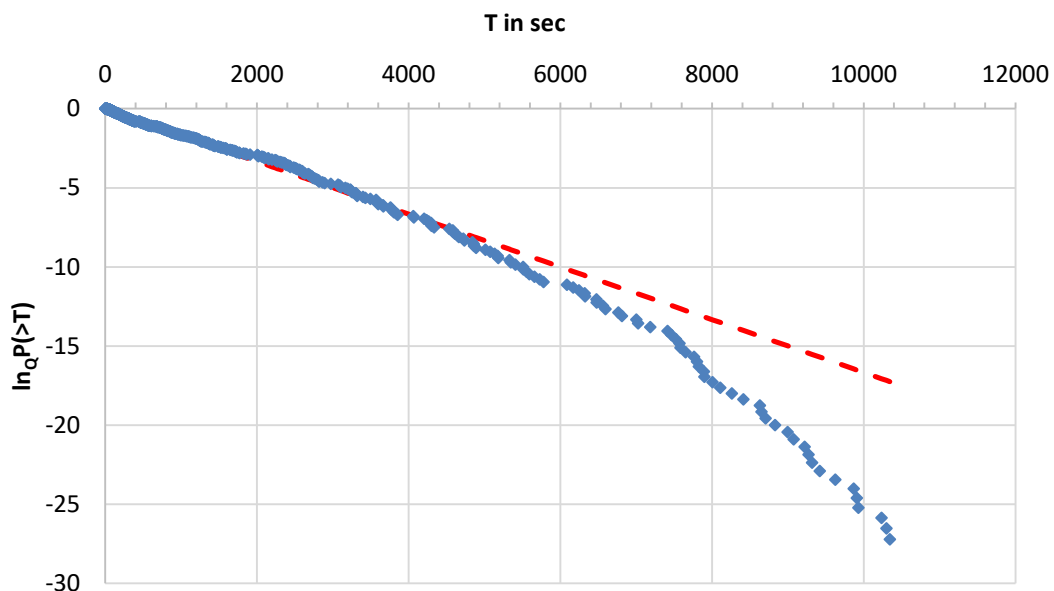
Figure 11: The Q-logarithmic function of the P (>T) as a function of the interevent times where the red line is the fitting with $q=1.62$. The deviation from the linearity suggests T_c values close to 7584 s.
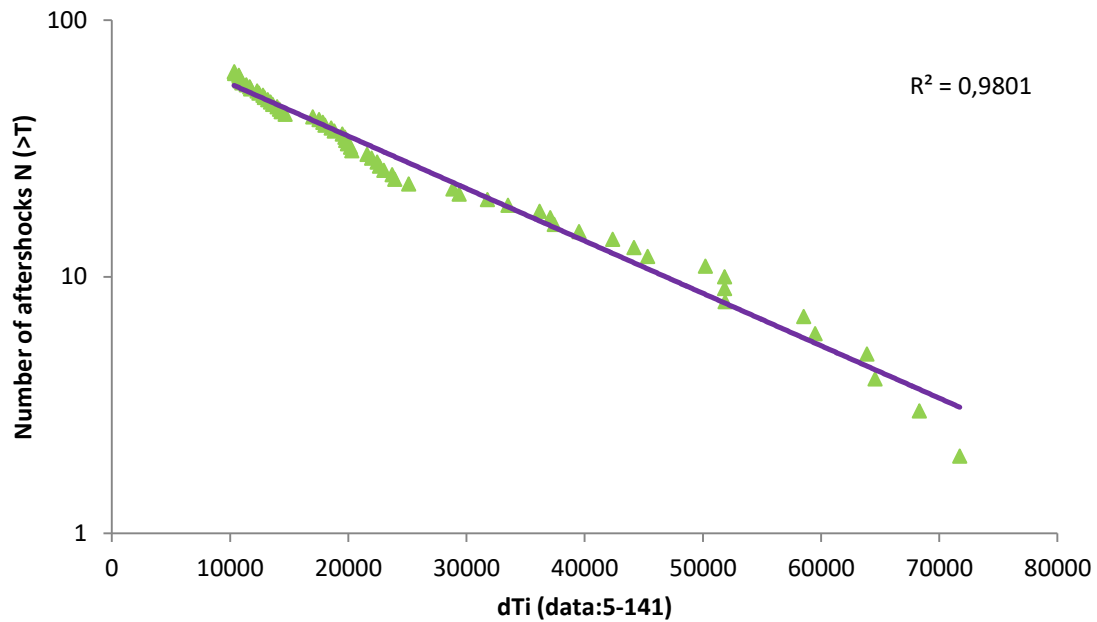
Figure 12: Diagram used to better estimate transition from one system to another. The results for the value of the T_c were based on the correlation coefficient, R^2.

Using the distribution observed (see Fig. 10) in conjunction with the image shown in the figure 11, the diagram in the figure 12 and the *q-value q = 1.62* acquired from our q-statistics fits, we lead to n≈1 meaning that the number of degrees of freedom.

Figure 13 presents the evolution of interevent time T as a function of time from the main event (in seconds). The T_c value (marked as the red line in Fig. 13) indicates that the majority of interevent times in the early aftershock time has T value less than T_c suggesting that the Tsallis entropy mechanism is predominant in the main part of the aftershock evolution while as the time evolves the characteristics of aftershock sequence for example, as that of finite degree of freedom and the long-range memory, related with a non-extensive statistical physics description are not more predominant and the Boltzmann–Gibbs (BG) statistical physics is recovered (i.e., q = 1) (Vallianatos F., Pavlou K., 2021).
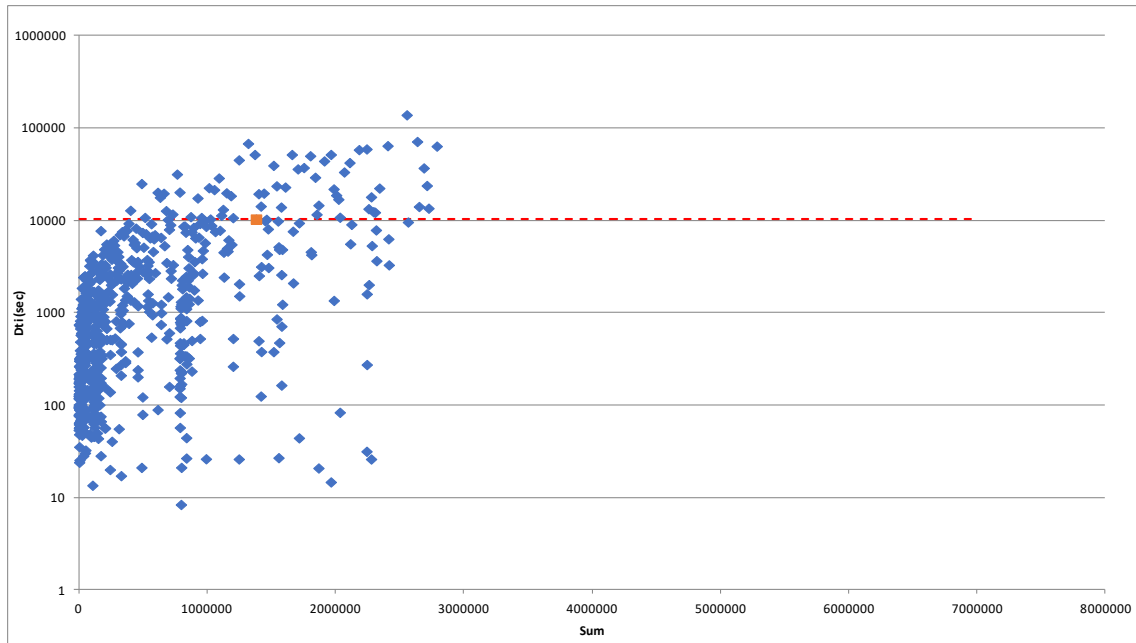
Figure 13: The evolution of interevent time *T* as a function of time t since the main event. The red line indicates the T_c value.

Next step is to examine the relationship between magnitude and time. The magni-tude-time pattern in the first weeks of the aftershock sequence can be seen if plotting the aftershock magnitude versus the logarithm of time t, after the mainshock and it is pre-sented in figure 14 below for the Elassona earthquake.
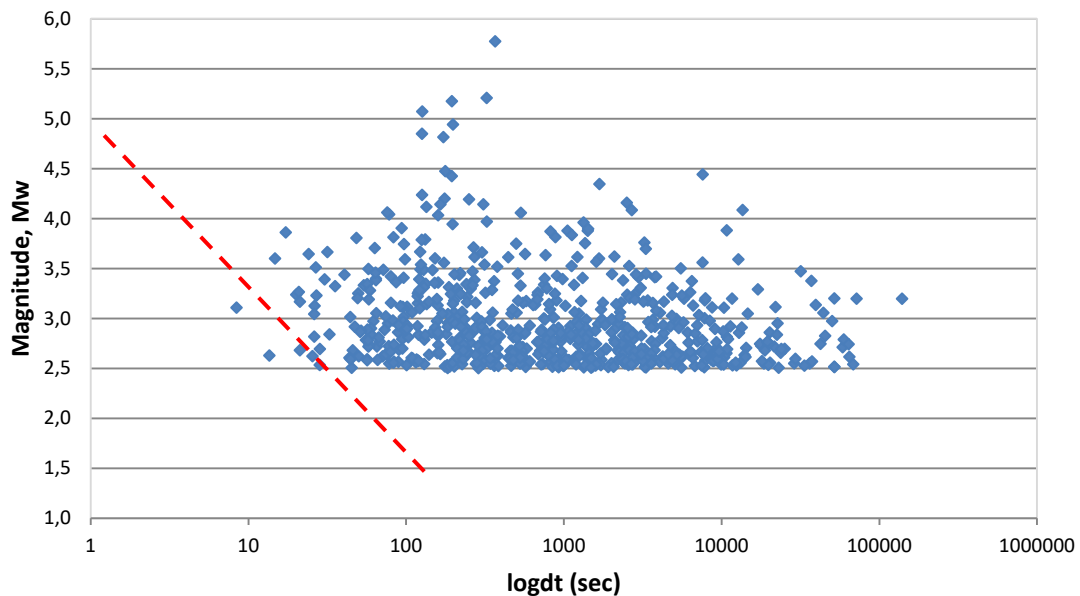

Figure 14: The magnitude-time pattern versus the logarithm of time.

Furthermore, we studied the distribution of magnitude based on Telesca's theory. In it, Telesca L. shows interest in the application of non-extensive models to the earthquake cumulative magnitude distribution (ECMD) by means of the maximum likelihood method. Non-extensivity in seismicity leads to a new form of the cumulative distribution of earthquake magnitudes, of which the

Gutenberg–Richter law can be considered as a particular case (Telesca L., 2012). To do this we used Matlab software as well as codes that calculated the parameters *qMag-value*, *ci-value* [showing confidence levels], *val-value*, parameter necessary for the calculation of the *qMag*. These codes were created by Michas G.

Figure 15 illustrates the log–linear plot of the magnitude function to N>M normalized to N. This distribution is characterized by a value *qMaq* equal to *qMag=1.54*.
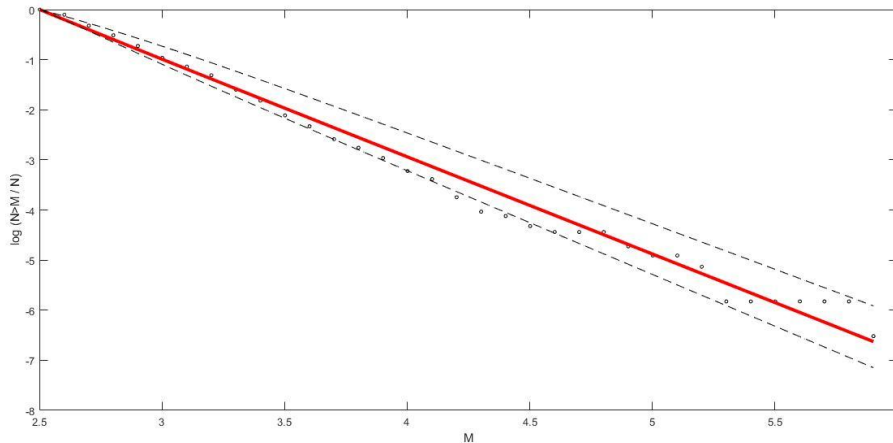
Figure 15: Magnitude distribution, $M>M_c$. The earthquake cumulative magnitude distribution showed in this figure (ECMD). The red line is fitting with *qMag=1.54*.

The results of the above analysis according to terms of Tsallis Entropy and the Theory of Telesca are summarized in the tables below.

val	-185,1374	
ci	1,5272-1,5585	-2525,7-2155,5
qMag	1,5428	

Table 4: Values of the various parameters resulting from the analysis of the magnitude distribution using the code '*qMag*Telesca'.

Event No.	Earthquake	Mc	Q	T*	qTime	T	qMag
1	Mytilene	2	3,11	1300	1,68	418,006	1,54
2	Kos	1,6	2,73	550	1,63	201,465	1,53
3	Zakynthos	2,1	3,13	5100	1,68	1629,393	1,54
4	Parnitha	1	3,46	3260	1,71	942,197	1,56
5	Elassona	2,5	2,6	600	1,62	230,77	1,54

Table 5: Values of the various parameters resulting from the analysis of the aftershocks sequences.

Event No.	Earthquake	Tc (sec)
1	Mytilene	42434
2	Kos	20997,2
3	Zakynthos	5607
4	Parnitha	175460
5	Elassona	7584,096

Table 6: Event No., Number of the event and T_c -value for the Tsallis entropy parameter of interevent time distribution which indicates that the majority of interevent times in the early aftershock time have T value less than T_c.

1.2. The 2019 Parnitha aftershock sequence

On 19th July 2019, at 11:13:15 GMT (Greenwich Mean Time) an earthquake of M_w=5.1 struck Athens, the Capital of Greece. The mainshock location parameters obtained from the catalogue of Kapetanidis V. et al. (2020), [the Seismological Laboratory of the National and Kapodistrian University of Athens (SL-NKUA)] are summarized in table 1. The main event is located at the coordinates (23.5265, 38.1291). The event occurred at the NW of the Thriassio basin (Kapetanidis V., et al., 2020). The aftershock distribution of the 436 events covers the region between the coordinates by longitudes 23.47°E- 23.67°E, and latitudes 38.05°N- 38.18°N and characterizes aftershocks with magnitudes $1.0 \leq M_w \leq 4.2$. The catalogue of this earthquake with completeness magnitude M_c=1.0, covers the period from the day of the main event to the 21st August of 2020. The distribution of the aftershock epicenters showed in the seismicity map below.
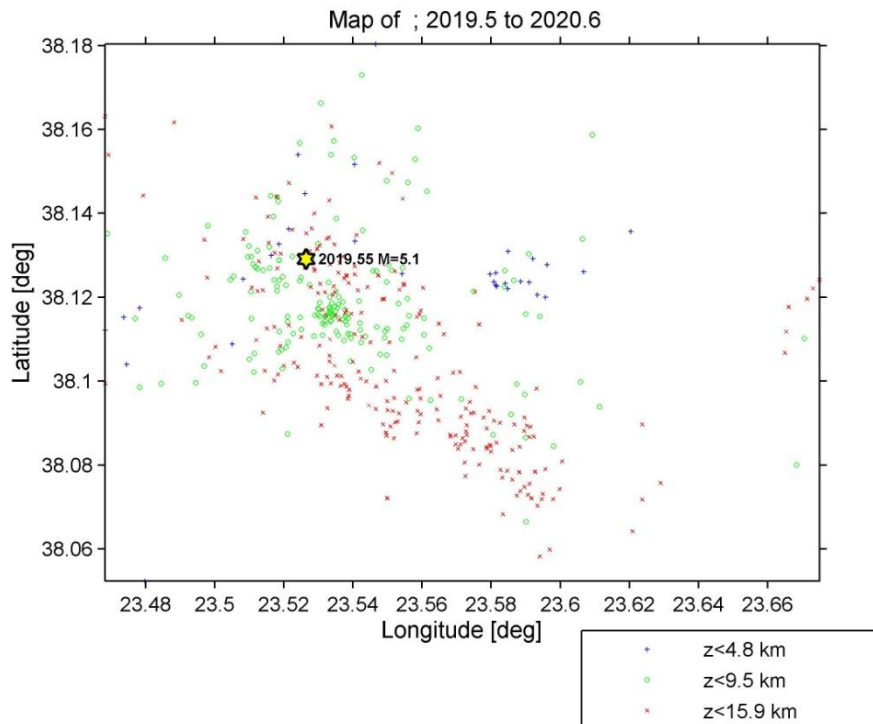
Figure 16: Epicenter distribution of the aftershock of Parnitha earthquake reported in the Kapetanidis et al., catalogue. Different depths of the aftershocks are given by different sizes and colors. The mainshock's epicenter symbolized the yellow star (this was made by applying the Z-map software package, v.6, Wiemer, 2001).

In the analyses related to space-time-magnitude distribution of the aftershocks, especially in the estimation of *b-value* and *p-value*, the use of complete data sets for all magnitude levels is quite important for reliable results in seismicity-based studies. So, for this reason, we used the maximum number of events. This occurs

by using the minimum magnitude of completeness M_c, the smallest magnitude that all the earthquakes are recorded, which is set above. M_c-value, based on the assumption of Gutenberg–Richter power law distribution of magnitudes can be estimated.

For the aftershock sequence of the Parnitha earthquake, we used the maximum likelihood estimation and the best combination of maximum curvature with M_c 95% and M_c 90% probability (Wyss M., Wiemer S., Zuniga R., 2001). Thus, M_c-value is selected as 1.0 in order to estimate the *b-value*, *a-value* and *p-value*.

The *b-value* is estimated as 0.73±0.05 and the *a-value* as 4.3.

As in the Elassona earthquake, we used two models in this earthquake so that we could describe the mode of aftershock decay as a function of time on frequency, which is modified by the Omori law. The values of the various parameters (*p-value*, *c-value*, *k-value*) describing these distributions are shown in Table 4 as well as in the figures below. Model 4 refers to the best RMS value, while model 2 refers to the best value of KS_statistics.

Earthquake Parnitha					
Best model (RMS)	**Value RMS**		**Best model (AIC-KS_statistics)**	**Value (AIC)**	**Value (KS_statistics)**
model 4	5,49		*model 2*	-837,7452	0,066667
p-value	**c-value**	**K-value**	**p-value**	**c-value**	**K-value**
p_1=1	c_1=10,128	k_1=529	p=0,9	c=0,097	k_1=27,4
p_2=0,84	c_2=0,135	k_2=17			k_2=15,2

Table 7: Parameters derived from the modified Omori law.
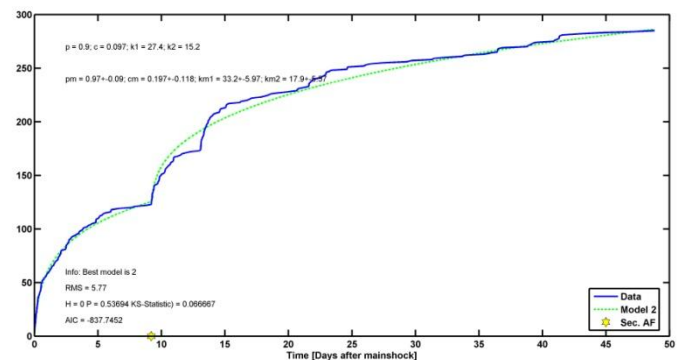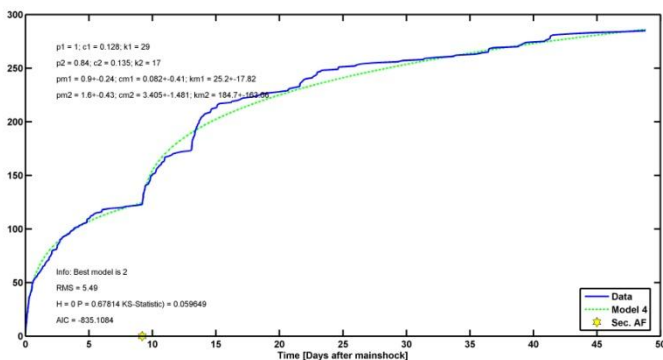
Figure 17,18: Number of aftershocks versus time (days after mainshock). The above two distributions result from the application of Omori law. More specifically, the left diagram shows the model 4 (best model RMS), while the corresponding model 2 (Best model (AIC-KS_statistics) is shown on the right. The estimated values for *p-value*, *c-value*, *k-value* are given in Table 7. It is worth commenting that in a time of about 10, 15, 22 days after the main earthquake, there is a step in the distribution. This is because aftershock sequences themselves have a complicated hierarchical structure in which each aftershock can produce its own aftershock sequence and so forth.
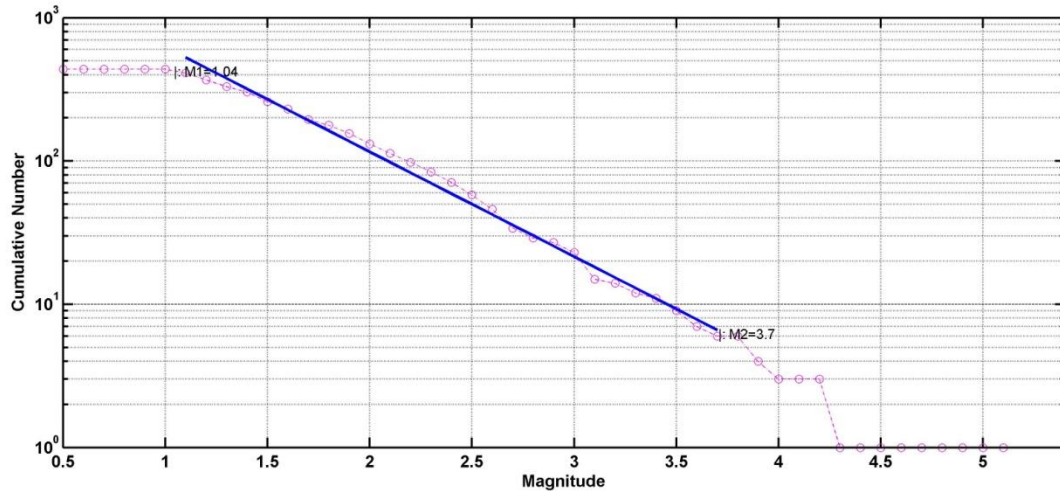
B-Value: 0.73

Standard Deviation: 0.05

Figure 19: The Guttenberg–Richter relation of aftershock sequence for Parnitha earthquake using the maximum likelihood method with the best combination of maximum curvature in a manual way (Mc 95% and Mc 90% probability). The estimated values for *b-value*, *a-value* their deviation and M_c are given in Table 3.

Next we tested the distribution of the interevent times in the aftershocks sequence of Parnitha based on the applied methodology in terms of Tsallis Entropy. We investigate the interval time T between two successful aftershocks. Figure 20 below shows the log–log plot of the cumulative distribution function (CDF) , $P(>T) = \frac{N(>T)}{N_0}$ of aftershocks interevent times which has a typical Q-exponential pattern. An inspection of Fig. 20 indicates that for large values of T ($T>T_c$ where T_c is a critical interevent time) a deviation from the Q-exponential is observed. Furthermore, a fitting of Q-exponential to the observed data, up to a value close to T_c, leads to *q=1.71* as you can see in table 5, in accordance with the equations (8), (9).The obtained value q ≈ 1.67 suggests a system with one degree of freedom. In the present aftershock sequence there is a slight increase in the parameter *q*. This is mainly due to the background seismicity.
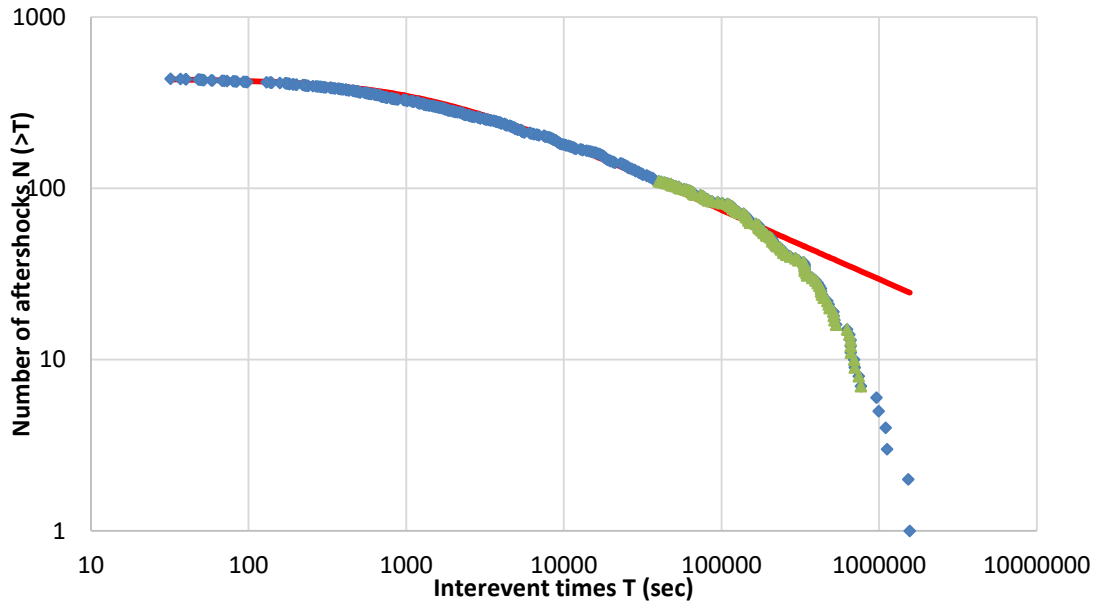
Figure 20: Interevent time distribution, *M>M_c.* The cumulative distribution functions of the interevent times for Parnitha earthquake. The red line is the q-exponential fitting with *q=1.71*.

Next, we represent the $\ln_Q P(> T)$ (see equation 10) as a function of interevent time *T* for *q=1.71,* in the figure 21. From the deviation from the expected linearity, the transition from one system to another we estimate that T_c has the value ≈175460 s. In this assessment we also took into consideration the correlation coefficient R2, as shown in figure 22. The data used to better calculate T_c are those shown with green triangles in Figure 20.
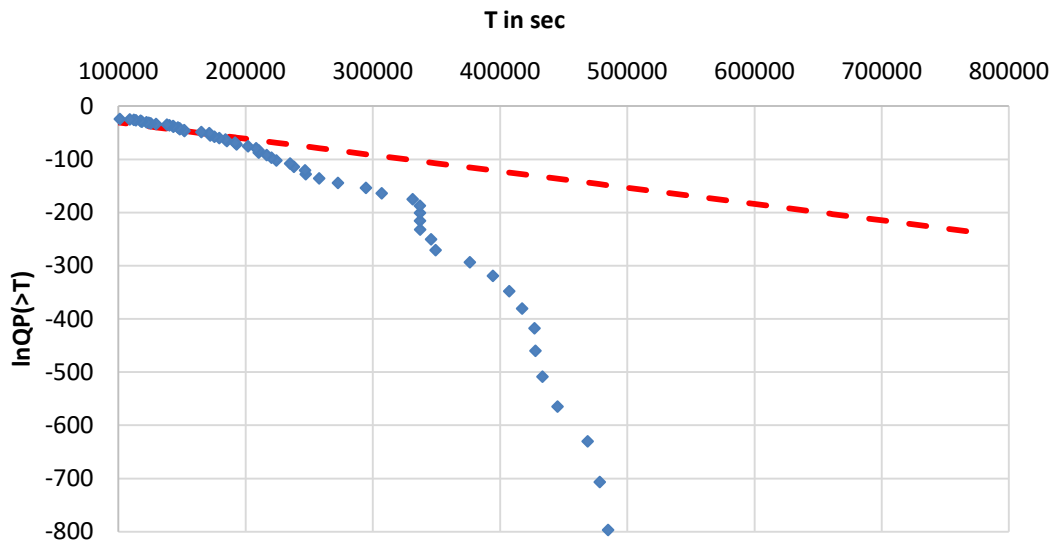
Figure 21: The Q-logarithmic function of the P (>T) as a function of the interevent times where the red line is the fitting with *q=1.71*. The deviation from the linearity suggests T_c values close to 175460 s.
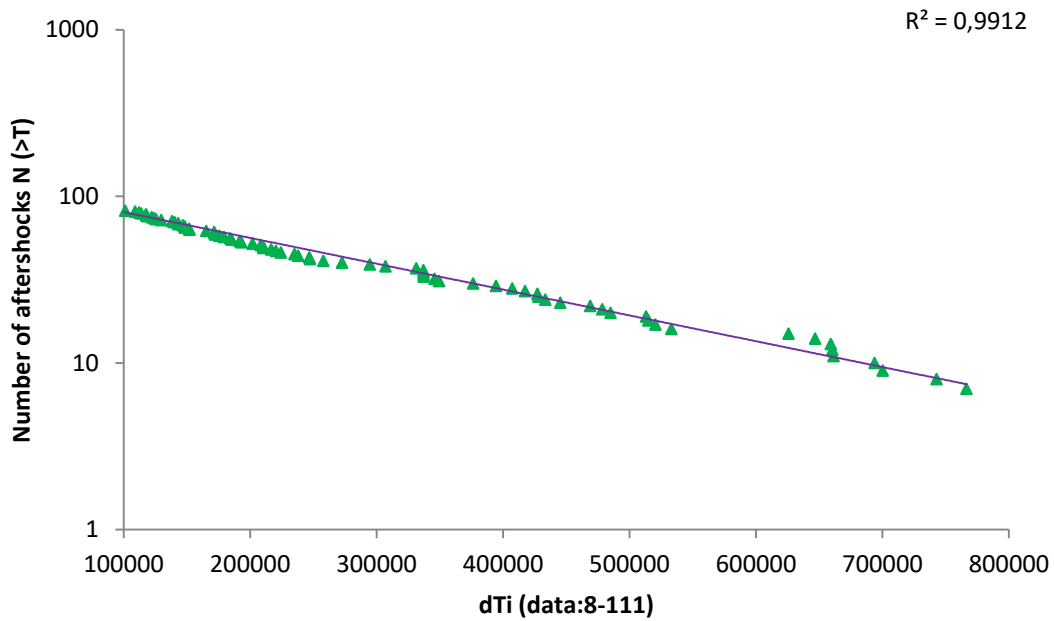
Figure 22: Diagram used to better estimate transition from one system to another. The results for the value of the T_c were based on the correlation coefficient, R^2.

In accordance with all of the above, we conclude that the q-value *q=1.71* acquired from our q-statistics fits, we lead to n≈1 meaning that the number of degrees of freedom.

In figure 23 we study the evolution of interevent time T as a function of time from the main event (in seconds). The T_c value was marked as the red line (see table 6).
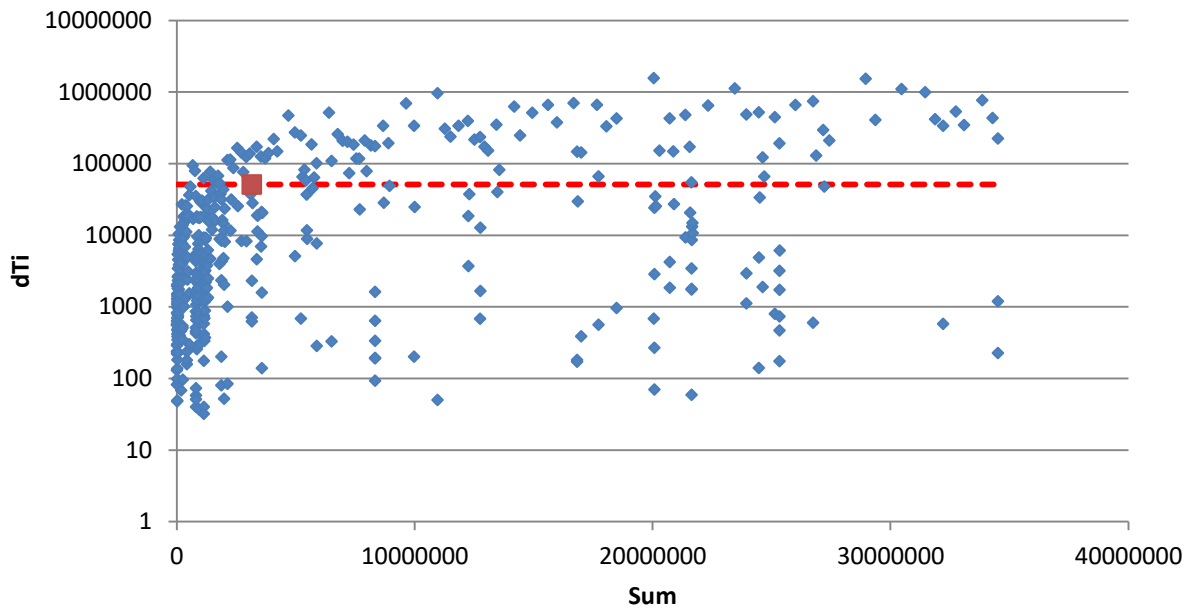
Figure 23: The evolution of interevent time T as a function of time t since the main event. The red line indicates the T_c value.

Next step is to examine the relationship between magnitude and time. The magnitude-time pattern in the first weeks of the aftershock sequence can be seen if plotting the aftershock magnitude versus the logarithm of time t, after the mainshock and it is presented in figure 24 below for the Parnitha earthquake. The dashed line indicates the so-called short-term aftershock incompleteness effect where the completeness magnitude M_c (t) depends logarithmically on the time Δτ since the mainshock and is given by the Kagan-Helmstetter expression (Kagan 2004; Helmstetter et al. 2005)[see more at Vallianatos F., Pavlou K., (2021), Scaling properties of the Mw7.0 Samos (Greece), 2020 aftershock sequence].
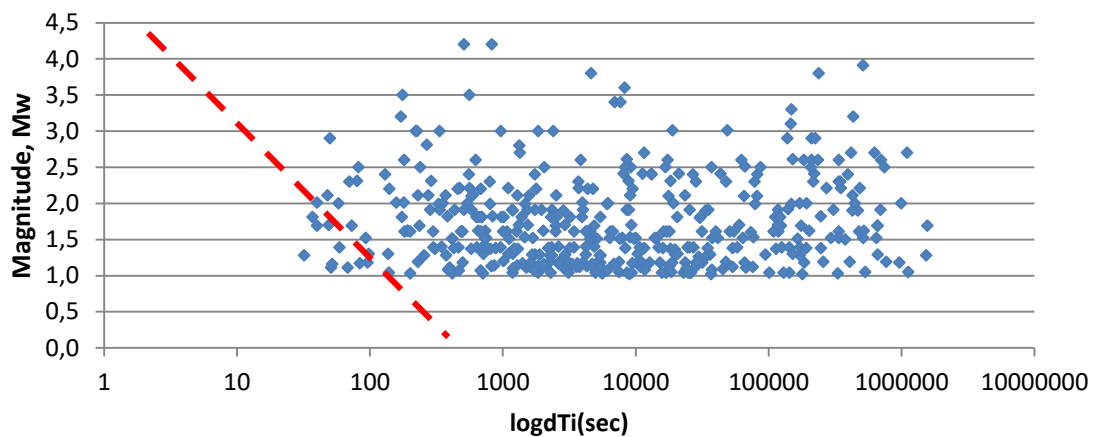
Figure 24: The magnitude-time pattern versus the logarithm of time.

Furthermore, we studied the distribution of magnitude based on Telesca's theory. In order to do this we used Matlab software as well as codes that calculated the parameters *qMag-value*, *ci-value* [showing confidence levels], *val-value*, parameter necessary for the calculation of the *qMag*. The results from this code are represented in the table 8.

Code qMagTelesca		
q$_{Mag}$	1,5556	
val	76,3786	
ci	1,5443-1,5669	32,9608-119,7964

Table 8: parameters *qMag-value*, *ci-value* [showing confidence levels], *val-value*.

Finally, figure 25 illustrates the log–linear plot of the magnitude function to N>M normalized to N. This distribution is characterized by a value *qMaq* equal to *qMag=1.56*.
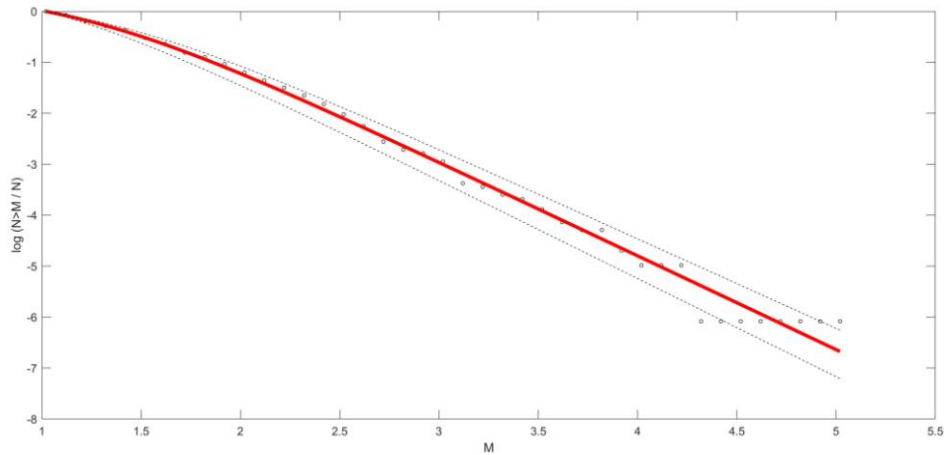
Figure 25: Magnitude distribution, *M>M$_c$*. The earthquake cumulative magnitude distribution showed in this figure (ECMD). The red line is fitting with *qMag=1.56*.

1.3. The 2018 Zakynthos aftershock sequence

We present an analysis of seismological data of the seismic sequence that started on October 25th, 2018 with a shallow $M_w = 6.6$ earthquake offshore Zakynthos (Ionian Sea, Greece). According to the publication of Ganas et al. (2020), the inversion of the Global Navigation Satellite System (GNSS) data shows the activation of an N-S striking thrust/oblique-slip fault at the African-Aegean plate interface with a length of ~26 km, and depth shallower than 15 km. The fault-plane geometry is well constrained by GNSS with a low-dip angle (23°), and dip-direction towards east. This is consistent with the distribution of the relocated aftershocks (1811 events). Their analysis indicates that the October 25, 2018 event ruptured the Hellenic megathrust. This event highlights the high degree of seismic coupling in the western region of the Hellenic Arc. It also highlights the "strong" nature of the subducting slab with the occurrence of "locked" patches under the Ionian seafloor that fail during large, reverse/oblique-slip earthquakes (Ganas et al., 2020).

More specifically with regard to this earthquake, the mainshock is located, as you can see in table 1, at the coordinates (20.4922, 37.3516). Based on detailed analysis of a 1668 aftershock sequence, which located by the station network of the Geodynamics Institute of the National Observatory of Athens (GI-NOA), the aftershock area, resulting from it, covers the region between the coordinates by longitudes 20.3594°E- 20.6268°E, and latitudes 37.2171°N- 37.4865°N. The observation days of the aftershocks are correspond to the 1-year time period i.e. from October 25th, 2018 up to October 19th, 2019. All data retrieved from the catalogue containing earthquakes of magnitude greater than or equal to the magnitude of completeness $M_w{\geq}M_c$. The completeness magnitude in this case is equal to M_c=2.1. As a result, our aftershocks are characterized by the magnitude of $2.1{\leq}M_w{\leq}5.5$.
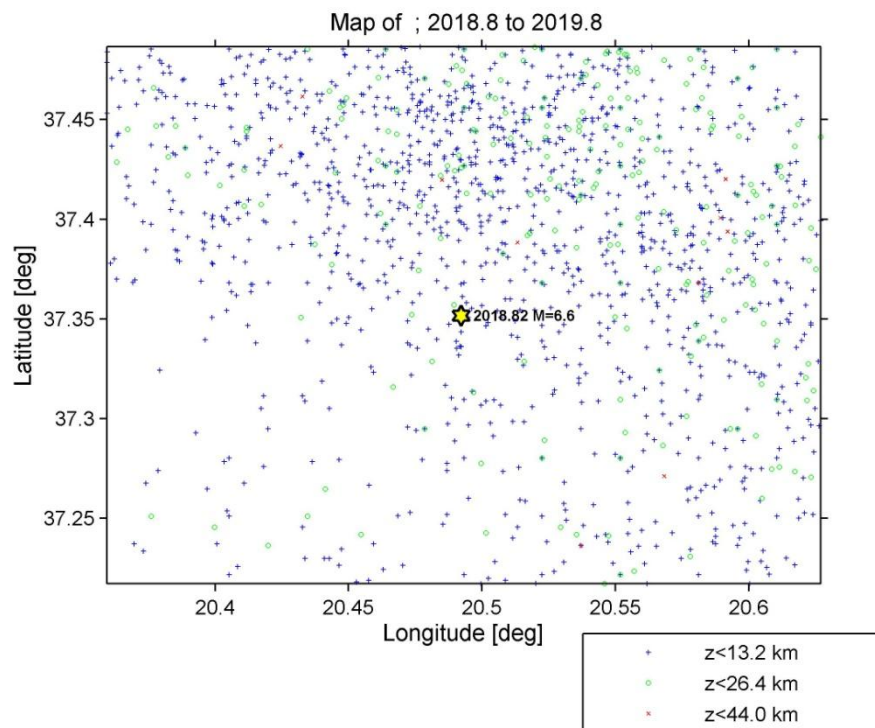
Figure 26: Epicenter distribution of the aftershock of Zakynthos earthquake reported in the NOA catalogue. Different depths of the aftershocks are given by different sizes and colors. The mainshock's epicenter symbolized the yellow star (this was made by applying the Zmap software package, v.6, Wiemer, 2001).

In order to study the statistical space-time-magnitude analysis for the aftershock sequence of October 25th, we estimated the *b-value* and the *a-value* from Gutenberg-Richter law and *p-value* from modified Omori law based on the completeness magnitude M_c. The *b-value* and its standard deviation were calculated as 1.04±0.1. However, it is well represented by the Gutenberg-Richter law with a typically b≈1.0. Also, the *a-value* estimated as 5.94.
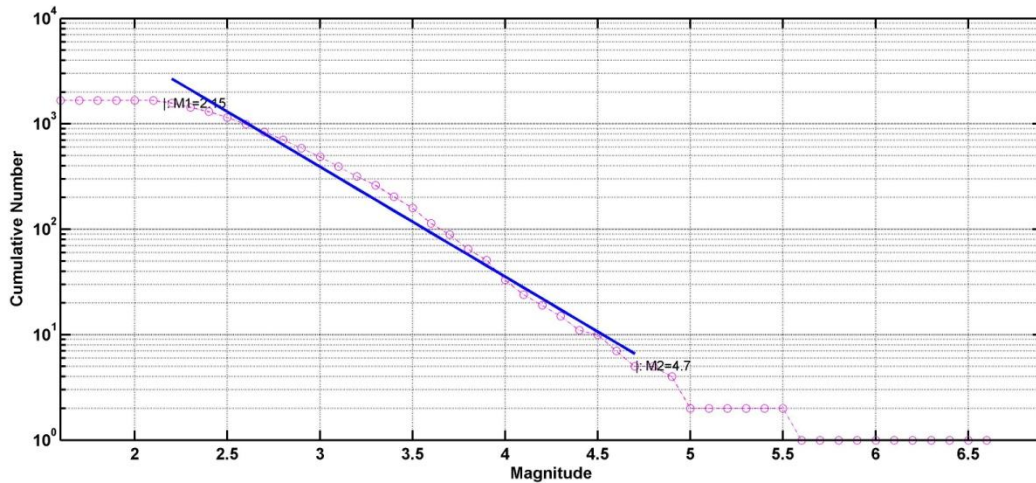
B-Value: 1.04

Standard Deviation: 0.1

Figure 9: The Guttenberg–Richter relation of aftershock sequence for Zakynthos earthquake using the maximum likelihood method with the best combination of maximum curvature in a manual way (Mc 95% and Mc 90% probability). The estimated values for *b-value*, *a-value* their deviation and M_c are given in Table 3.

With regard to the modified Omori's law for the temporal decay of aftershocks we present two models out of four. In this aftershock sequence the best models are model 4 and model 3.

Earthquake Zakynthos					
Best model (RMS)	**Value RMS**		**Best model (AIC-KS_statistics)**	**Value (AIC)**	**Value (KS_statistics)**
model 4	8,37		*model 3*	-2877,9683	0,032808
p-value	**c-value**	**K-value**	**p-value**	**c-value**	**K-value**
p_1=0,63	c_1=2,3	k_1=89,4	p_1=0,58	c=1,463	k_1=72,2
p_2=1,91	c_2=1,364	k_2=69,7	p_2=1,7		k_2=67,8

Table 9: Parameters derived from the modified Omori law.

In the first diagram, we select the model that displays a lower RMS value, while in the second case we attach the model that is engraved by the smallest value KS_statistics. Model 4 refers to the best RMS value, while model 3 refers to KS_statistics. Thus, each time different values of the parameters *p-value*, *c-value*, *k-value* arise depending on the model that best meets our requirements. These various values are summarized in the table above.
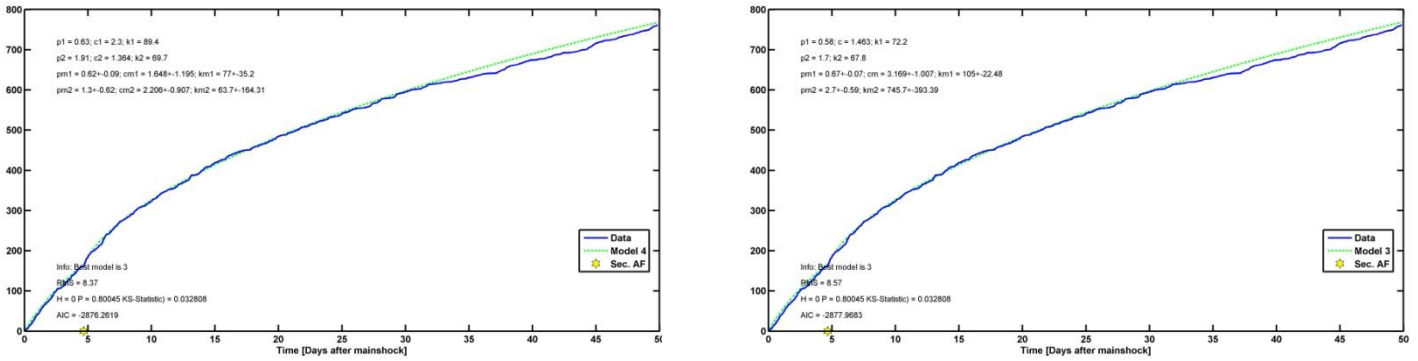
Figure 28,29: Number of aftershocks versus time (days after mainshock). The above two distributions result from the application of Omori law. More specifically, the left diagram shows the model 4 (best model RMS), while the corresponding model 3 (Best model (AIC-KS_statistics) is shown on the right. The estimated values for *p-value*, *c-value*, *k-value* are given in Table 9.

As in the two previous cases, so in this aftershock sequence, we investigate the distribution of the interevent times between two successful aftershocks in terms of Tsallis Entropy. The log–log plot of the CDF, $P(>T) = \frac{N(>T)}{N_0}$ of aftershocks interevent times which has a typical Q-exponential pattern has shown in figure 29. From this, we found out that the value of T_c is close to *q=1.68* as you can see in table 5, in accordance with the equations (8), (9). The obtained value q ≈ 1.67 suggests a system with one degree of freedom; therefore we are talking about such a system.
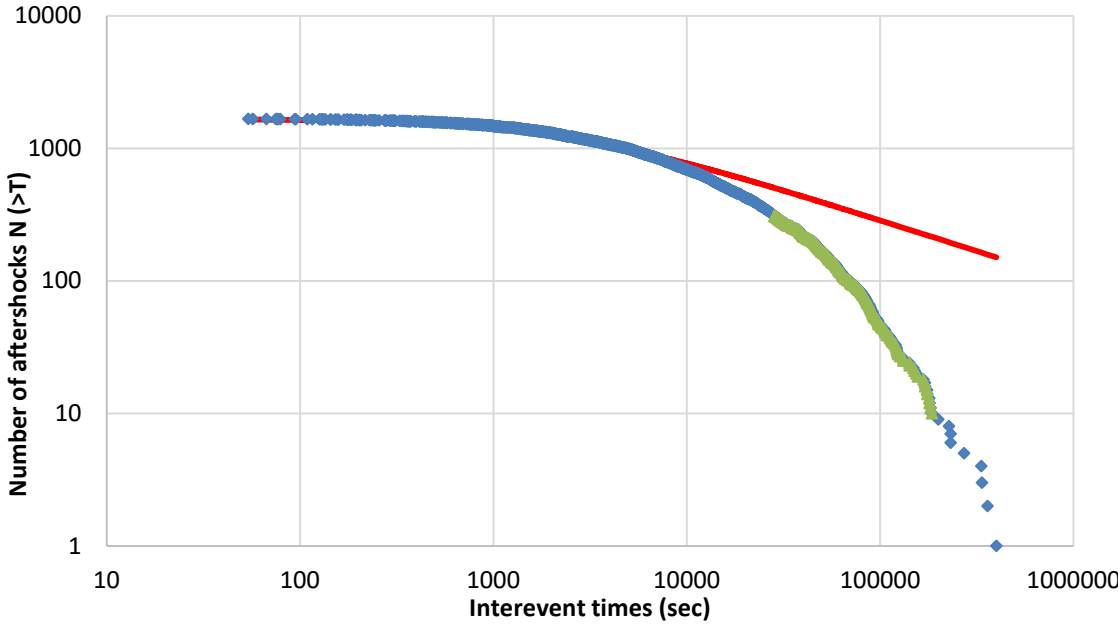
Figure 30: Interevent time distribution, *M>M$_c$*. The cumulative distribution functions of the interevent times for Zakynthos earthquake. The red line is the q-exponential fitting with *q=1.68*.

In the figure 31, is represented the $\ln_Q P(>T)$ (see equation 10) as a function of interevent time *T* for *q=1.68*. The transition from one system to another, from the deviation from the expected linearity, we estimate that T_c has the value ≈5607 s. We also took into consideration the correlation coefficient R², as shown in the

figure 32. The data used to better calculate T_c are those shown with green triangles in Figure 33.
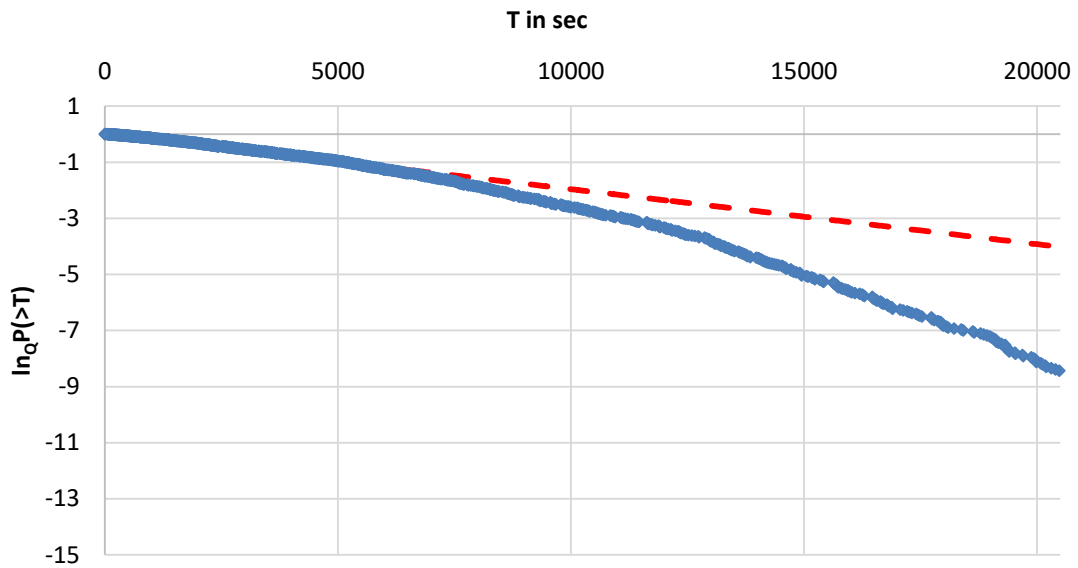

Figure 31: The Q-logarithmic function of the P (>T) as a function of the interevent times where the red line is the fitting with _q=1.68_. The deviation from the linearity suggests T_c values close to 5607 s.
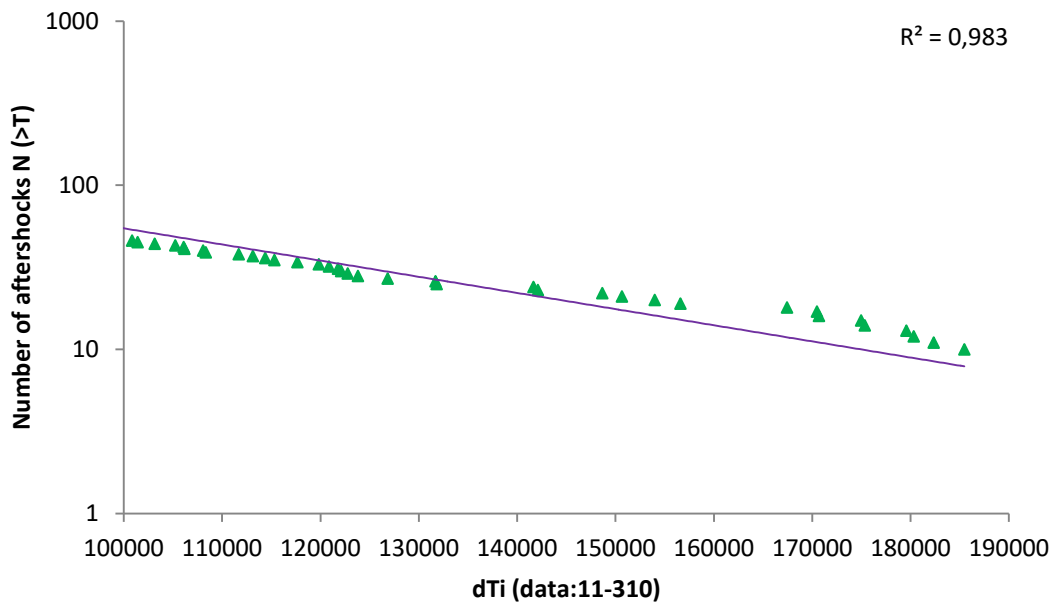

Figure 32: Diagram used to better estimate transition from one system to another. The results for the value of the T_c were based on the correlation coefficient, R^2.

In figure 33 we study the evolution of interevent time T as a function of time from the main event (in seconds). The T_c value was marked as the red line (see table 6).
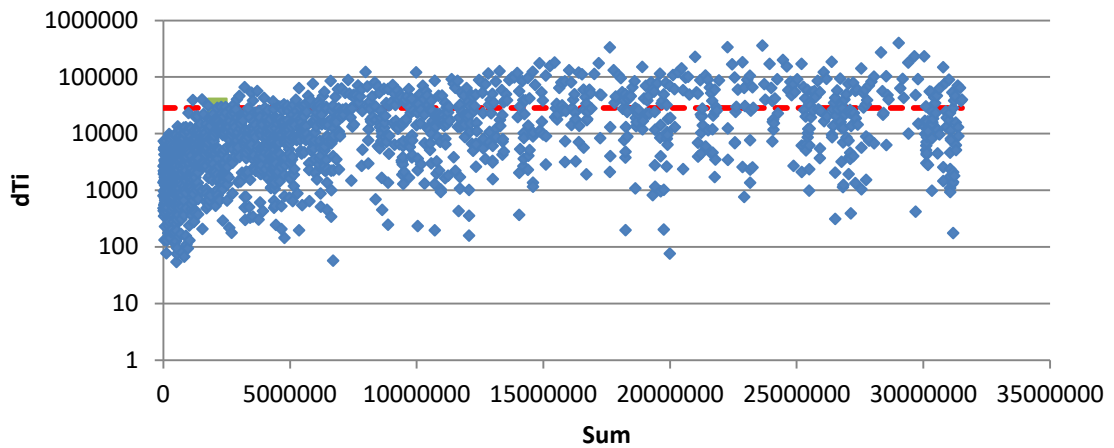
Figure 33: The evolution of interevent time T as a function of time t since the main event. The red line indicates the T_c value.

The magnitude-time pattern in the first weeks of the aftershock sequence can be studied if we plot the aftershock magnitude versus the logarithm of time t, after the mainshock and it is presented in figure 34. The dashed line indicates the short-term aftershock incompleteness effect where the completeness magnitude M_c (t) depends logarithmically on the time Δτ since the mainshock (Vallianatos F., Pavlou K., 2021)
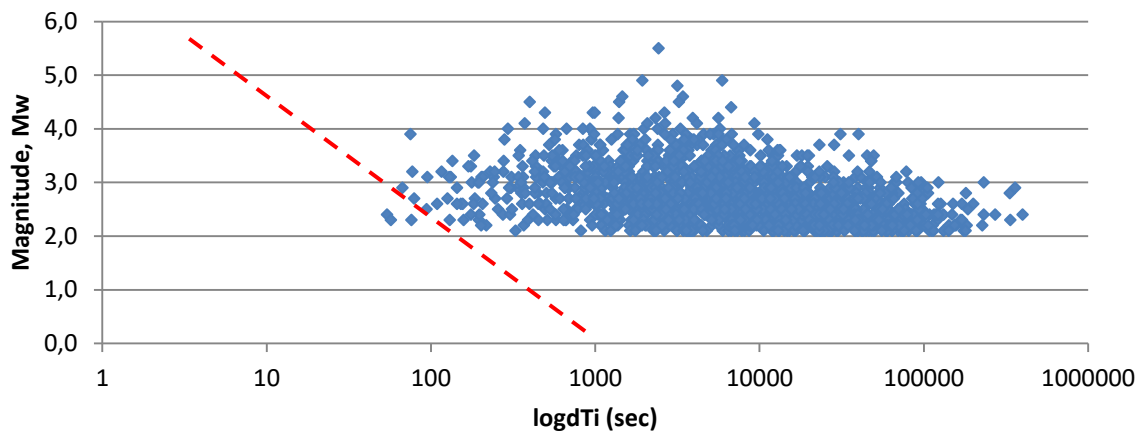
Figure 34: The magnitude-time pattern versus the logarithm of time.

The distribution of magnitude based on Telesca's theory, it's also taken into examination. The below parameters were obtained by using the code from Michas G. The results from this code are represented in table 9.

Code qMagTelesca			
q$_{Mag}$	1,5403		
val	25,4965		
ci	1,5198-1,5608	-342,6605	up to 393,6535

Table 9: parameters qMag-value, ci-value, val-value

At last, figure 35 displays the log–linear plot of the magnitude function to N>M normalized to N. This distribution is characterized by a value *qMaq* equal to *qMag=1.54*.
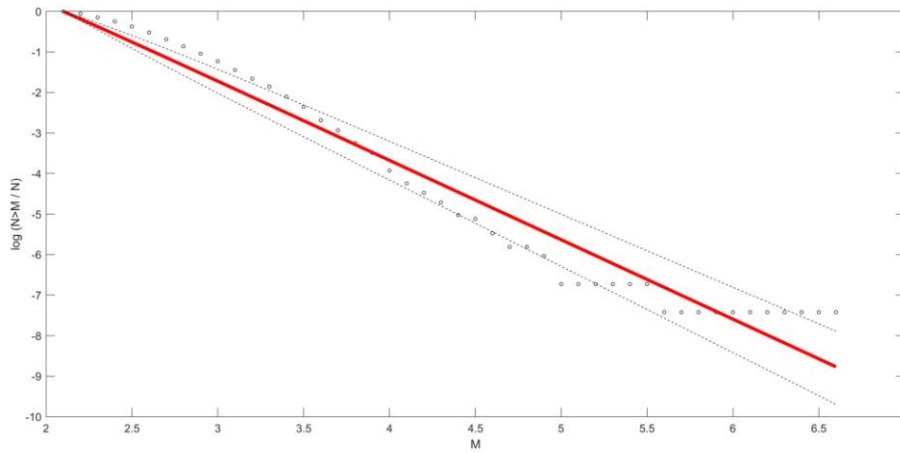

Figure 35: Magnitude distribution, *M>M$_c$*. The earthquake cumulative magnitude distribution showed in this figure (ECMD). The red line is fitting with *qMag=1.54*.

1.4. The 2017 Kos aftershock sequence

An earthquake with local magnitude *M$_L$*=6.6 at a depth of 7.1 km which has a normal faulting mechanism striking about east-west occurred on July 20, 2017 in Gökova Bay, in Aegean Sea, at 22:31:10 GMT between Bodrum town, Turkey, and Kos Island, Greece. According to the data, the mainshock epicenter was 27.4057°E and 36.9693°N located 12 km to Kos in Greece and 8 km to Bodrum in Muğla in Turkey. The earthquake caused a tsunami which affected the coast of Bodrum peninsula and the northeast coast of Kos Island. The tsunami was recorded by a tide gauge, located in Bodrum, close to the earthquake epicenter (Öztürk S., Şahin S., 2018).

The data were obtained from the Boun Koeri Regional Earthquake-Tsunami Monitoring Center, Kandilli Observatory and Earthquake Research Institute (RETMC) [the Turkish Disaster and Emergency Management Presidency, AFAD; Boğaziçi University (KOERI)]. The coordinates of the study area are by longitudes 27.0015°E-27.9937°E, and latitudes 36.7015°N-37.0745 °N. The objective of this study is to present a detailed region-time-magnitude analysis including several aftershock parameters such as the *b-value* of the frequency-magnitude distribution, the *p-value* of the modified Omori law and parameter q

by Tsallis for 6492 aftershocks identified in six months after the mainshock. Based on the seismicity map of the aftershock epicenters, the aftershock catalogue was characterized by magnitudes $1.6 \leq M_L \leq 5.1$. From this we understand that the completeness magnitude is equal to $M_c=1.6$. All calculations of aftershock parameters *b-value*, *p-value*, and *Mc* were made by applying the Z-map software package. More information about the values of the parameters mentioned above can be seen in table 3 as well as in table 6. However, it is worth noting that in this particular Bodrum-Kos earthquake the detailed analysis of the aftershock sequence, regarding the law of Omori, arises a model that simultaneously covers both our requirements and constitutes the exception compared to the other cases of earthquake analysis in this paper. In any case, the best model is considered the model 4. *P-value* is estimated as *p-value* ≈0.9 and is well characterized nearly close to global p ≈1.0. This relatively low *p-value* may be a result of the relative slow decay rate of the aftershock activity.

Earthquake Kos					
Best model (RMS)	**Value RMS**		**Best model (AIC-KS_statistics)**	**Value (AIC)**	**Value (KS_statistics)**
model 4	86,33		*model 4*	-36567,1466	0,041973
		p-value	**c-value**	**K-value**	
		$p_1=0,88$	$c_1=0,957$	$k_1=845,5$	
		$p_2=1,62$	$c_2=0,393$	$k_2=137,6$	

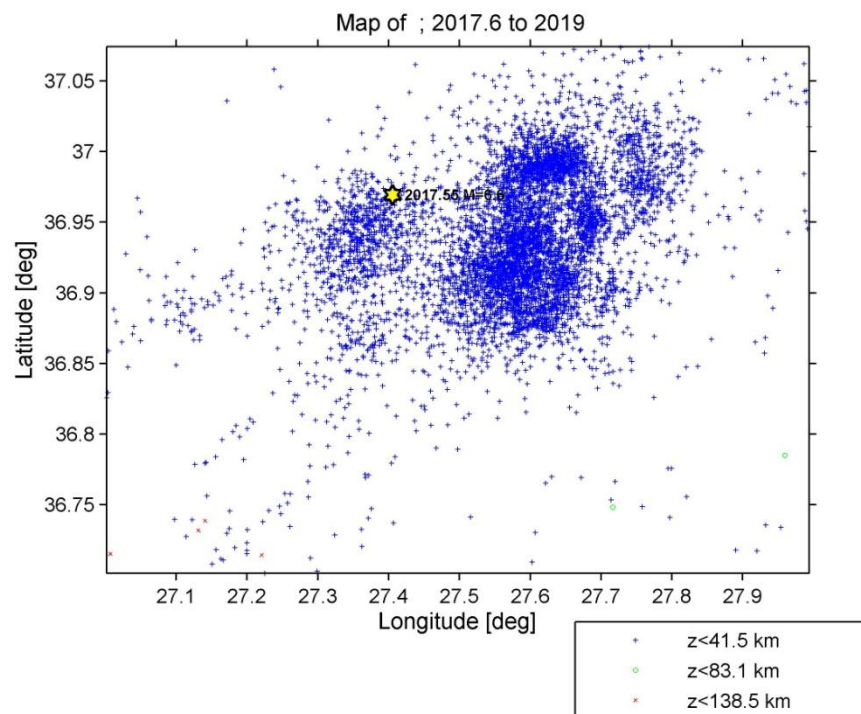**Table 10: Parameters derived from the modified Omori law.**

Figure 36: Epicenter distribution of the aftershock of Kos-Turkey earthquake reported in the Boun Koeri Regional Earthquake-Tsunami Monitoring Center, Kandilli Observatory and Earthquake Research Institute (RETMC) catalogue. Different depths of the aftershocks are given by different sizes and colors.

The mainshock's epicenter symbolized the yellow star (this was made by applying the Z-map software package, v.6, Wiemer, 2001).
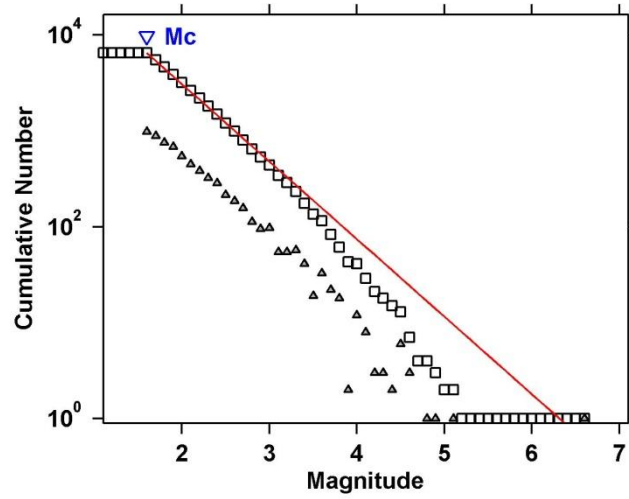
Maximum Likelihood Solution
b-value = 0.808 +/- 0.009, a value = 5.11, a value (annual) = 4.9
Magnitude of Completeness = 1.6

Figure 37: The Guttenberg–Richter distribution for Budrum-Kos earthquake using the maximum likelihood method with the best combination of maximum curvature (Mc 95% and Mc 90% probability). The estimated values for *b-value*, *a-value* and M_c are given in Table 3.
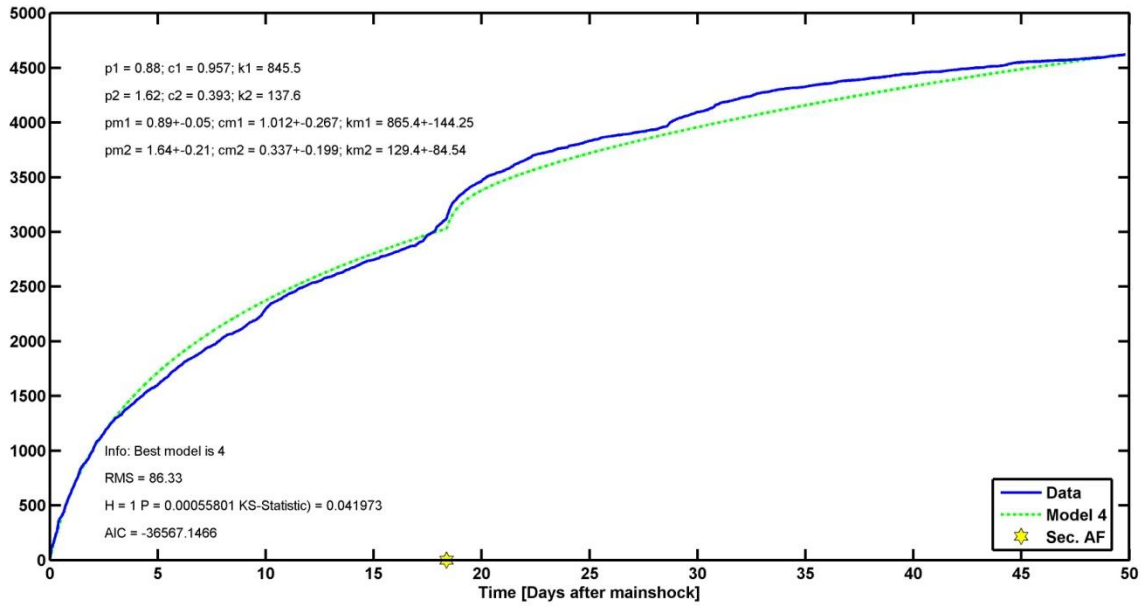
Figure 38: Number of aftershocks versus time (days after mainshock). The above distribution result from the application of Omori law. More specifically, this diagram shows the model 4 that simultaneously covers both our requirements (best model RMS and best model (AIC-KS_statistics). The estimated values for *p-value*, *c-value*, *k-value* are given in Table 10. It is worth commenting that in a time of about 18-19 days after the main earthquake, there is a step in the distribution. This is because aftershock sequences themselves have a complicated hierarchical structure in which each aftershock can produce its own aftershock sequence and so forth.

In terms of Tsallis Entropy, we study the distribution of the interevent times between two successful aftershocks. The log–log plot of the CDF , $P(> T) = \frac{N(>T)}{N_0}$ of aftershocks interevent times has a typical Q-exponential pattern which is shown in figure 39. The value of *q* is equal to *q=1.63* as you can see in table 5, according to the equations (8), (9).
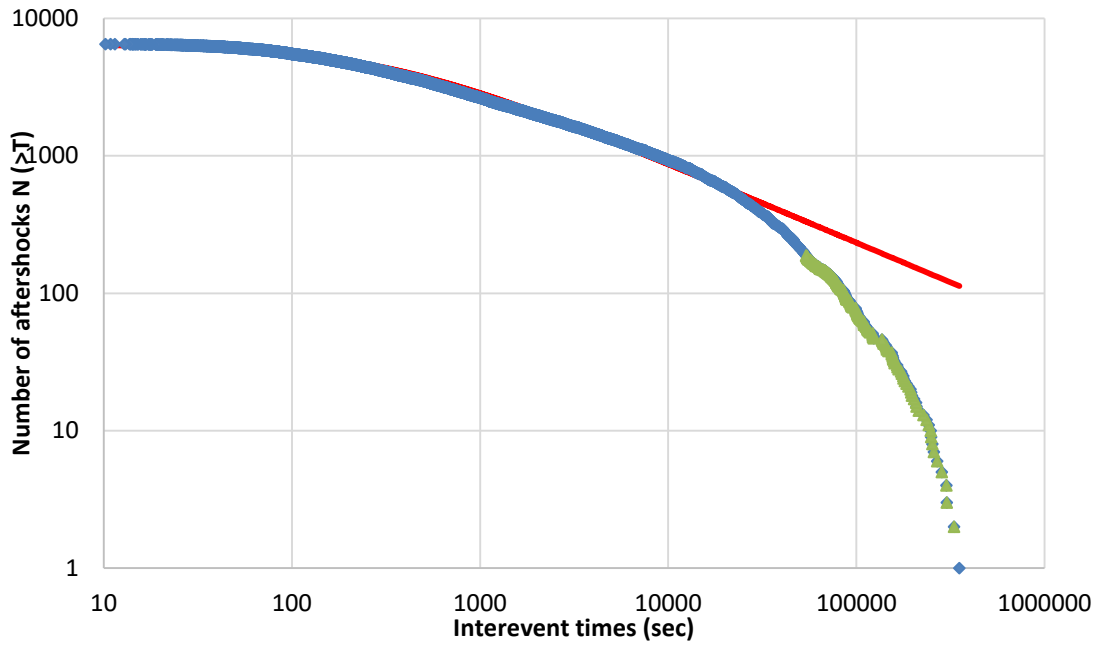
Figure 40: Interevent time distribution, *M>M_c*. The cumulative distribution functions of the interevent times for Kos earthquake. The red line is the q-exponential fitting with *q=1.63*.

Following, we have the $\ln_Q P(>T)$ as a function of interevent time *T* for *q=1.63*. The transition from one system to another, estimated to be at $T_c \approx 20997$ s. We also took into consideration the correlation coefficient R^2, as shown in figure 42. The data used to better calculate T_c are those shown with green triangles.
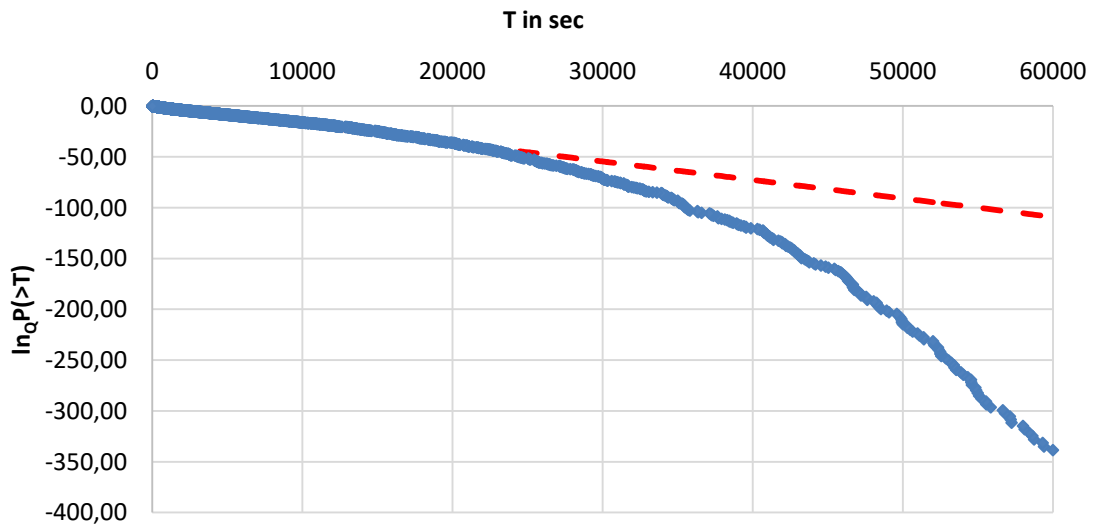
Figure 41: The Q-logarithmic function of the P (>T) as a function of the interevent times where the red line is the fitting with *q=1.63*. The deviation from the linearity suggests T_c values close to 20997 s.
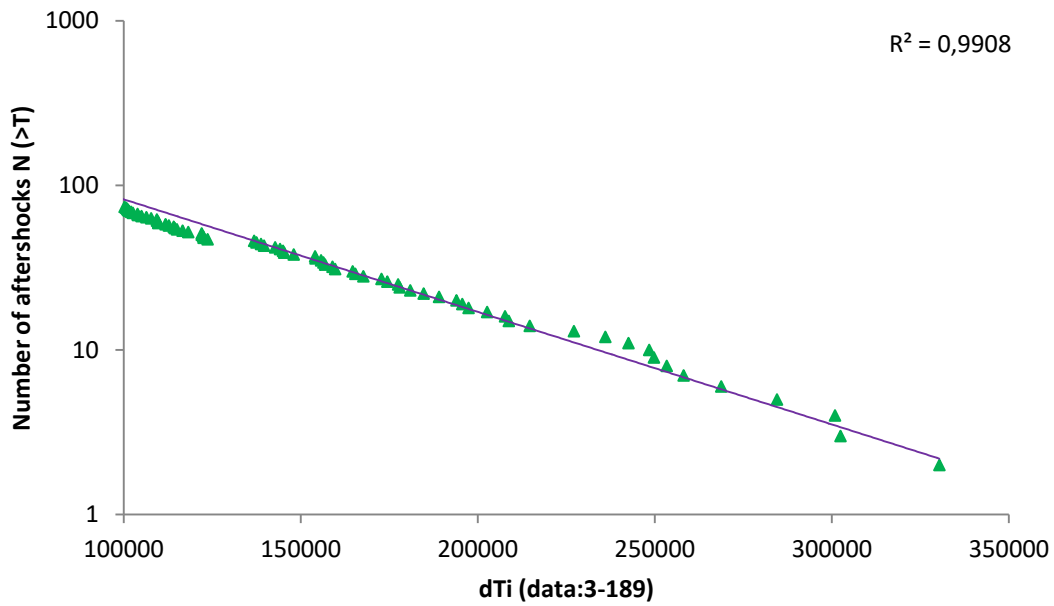
R² = 0,9908

Figure 42: Diagram used to better estimate transition from one system to another. The results for the value of the T_c were based on the correlation coefficient, R^2.

In the following figure, we study the evolution of interevent time T as a function of time from the main event (in seconds). The T_c value was marked as the red line (see table 6).
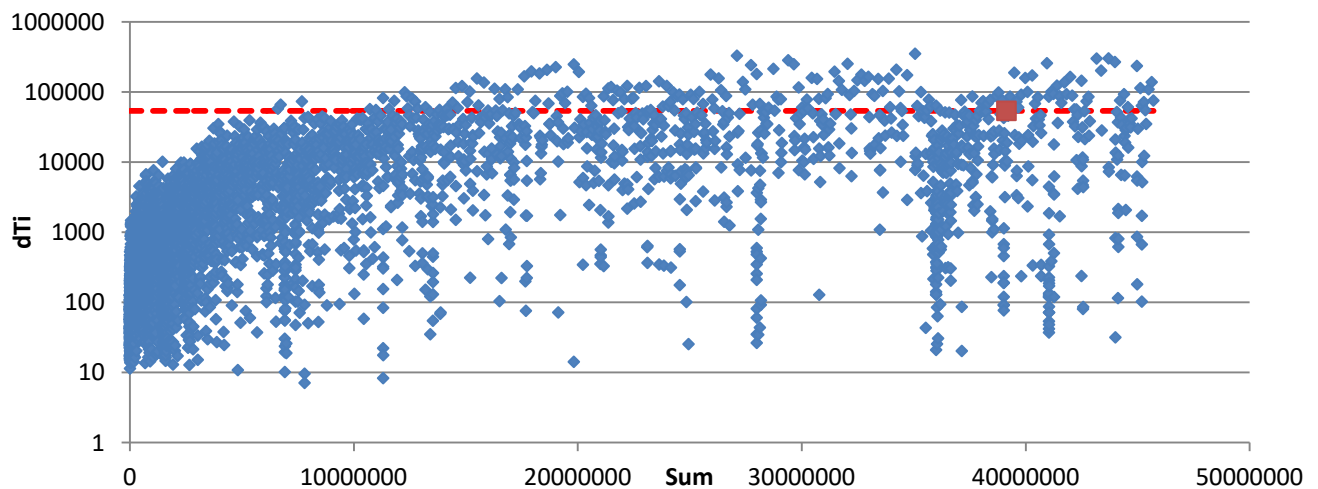

Figure 43: The evolution of interevent time T as a function of time t since the main event. The red line indicates the T_c value.

By plotting the aftershock magnitude versus the logarithm of time t, after the mainshock, we can study the magnitude-time pattern in the first weeks of the aftershock sequence. The dashed line illustrates the short-term aftershock incompleteness effect (Vallianatos F., Pavlou K., 2021).
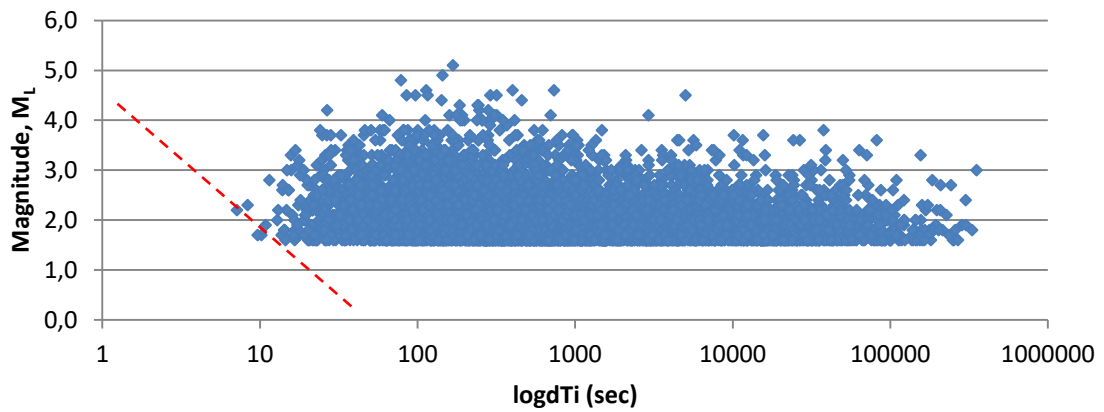
Figure 44: The magnitude-time pattern versus the logarithm of time.

The below parameters were obtained by using the Matlab code based on Telesca's theory about the distribution of magnitude. The results are represented in table 10. Finally, figure 45 displays the log–linear plot of this distribution which is characterized by a value *qMaq* equal to *qMag=1.52*.

Code qMagTelesca			
q_{Mag}	1,5267		
val	-3,9858		
ci	1,5093-1,5441	-117,6823	up to 109,7108

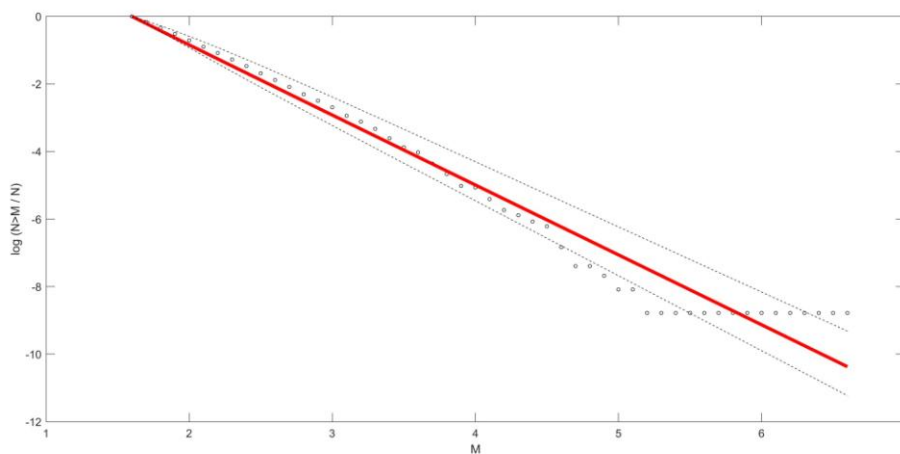**Table 10: parameters *qMag-value*, *ci-value*, *val-value*.**

Figure 45: Magnitude distribution, *M>M_c.* The earthquake cumulative magnitude distribution showed in this figure (ECMD). The red line is fitting with *qMag=1.52*.

1.5. The 2017 Mytilene aftershock sequence

The 2017 Mytilene earthquake, M_w 6.3, was recorded by the European Mediterranean Seismological Centre (EMSC). This earthquake took place at the coordinates (26.31, 38.85) (see more for location parameters in the table 1) on 12th of June at 12:28:37 GMT. This offshore destructive event occurred approximately 15 km south of the SE coast of Lesvos Island, NE of Chios. There was one fatality in Vrissa village, caused by building collapse and fifteen people were injured due to collapsing buildings and falling debris. Damage was widespread throughout the southeastern part of Lesvos (damage is reported in at least 12 villages) whereas effects have been also observed at the Turkish coast (Lekkas E. et al., 2017). As regards the induced earthquake environmental effects, slope movements and ground cracks were generated in many sites of the affected area as well as seismic waves (tsunami) were reported in Plomari port.

A total of 1610 aftershocks were detected over the period between 12 June 2017 and 11 June 2018. The aftershock area covers the region between the coordinates by longitudes 25.22°E-27.30°E, and latitudes 38.23°N-39.22°N. Figure 46 shows the seismicity map, especially the distribution of the aftershock epicenters. Aftershock catalogue was characterized by magnitudes $2.0 \leq M_w \leq 5.2$. From this we understand that the completeness magnitude is equal to M_c=2.0.
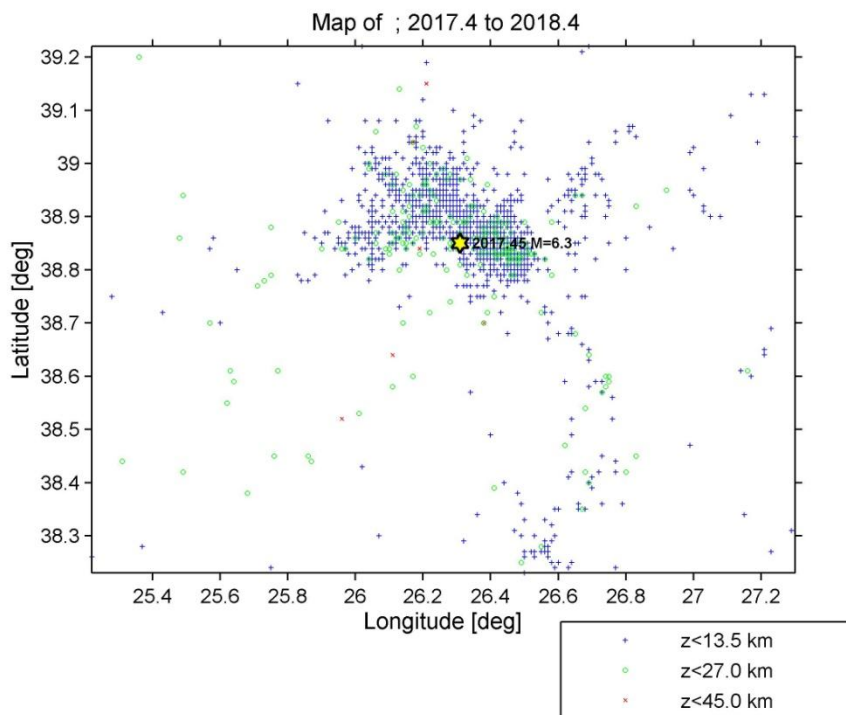

Figure 46: Epicenter distribution of the aftershock of Mytilene earthquake reported in the AUTH catalog. Different depths of the aftershocks are given by different sizes and colors. The mainshock's epicenter symbolized the yellow star (this was made by applying the Z-map software package, v.6, Wiemer, 2001).
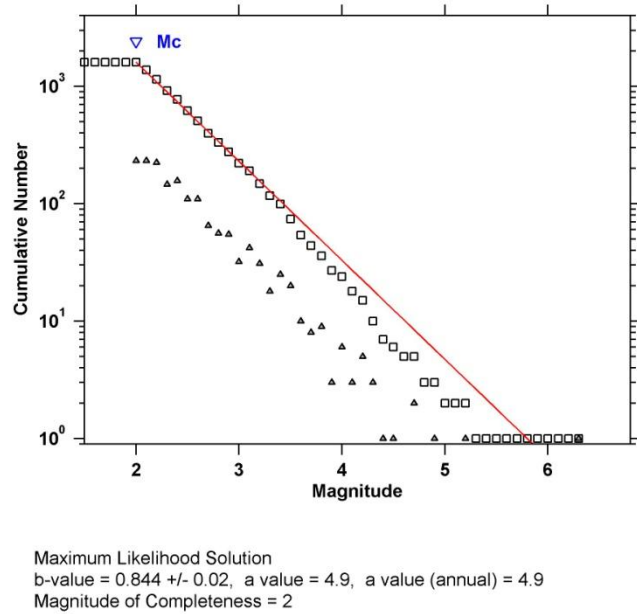
Maximum Likelihood Solution
b-value = 0.844 +/- 0.02, a value = 4.9, a value (annual) = 4.9
Magnitude of Completeness = 2

Figure 47: The Guttenberg–Richter distribution for Mytilene earthquake using the maximum likelihood method with the best combination of maximum curvature (Mc 95% and Mc 90% probability). The estimated values for *b-value*, *a-value* and M_c are given in Table 3.

The analysis was focused on a first analysis of the scaling properties observed in the aftershock sequence. The aftershock sequence follows the Gutenberg and Richter law. The *a-value* and *b-value* came out, as in previous cases of aftershock sequences, with the completeness magnitude M_c using the maximum likelihood estimation and the best combination of maximum curvature with M_c 95% and M_c 90% probability, resulting from using the Z-map software. These two parameters and their standard deviations take values *b-value*= 0.844±0.02 and *a-value*= 4.9, respectively. However, to study the time distribution of the aftershocks we use the modified Omori law. The parameter *p-value* is the most important parameter which defines the mode of aftershock decays as a function of time on frequency, since the aftershock sequence obeys also the Omori law. On this occasion, we end up with the two best models. In the first case, we select the model that displays a lower RMS value, while in the second case we attach the model that is engraved by the smallest value KS_statistics. Model 4 refers to the best RMS value, while model 2 refers to KS_statistics. Thus, each time different values of the parameters *p-value, c-value, k-value* arise depending on the model that best meets our requirements. These various values are summarized in the table 11 below.

Earthquake Mytilene					
Best model (RMS)	**Value RMS**		**Best model (AIC-KS_statistics)**	**Value (AIC)**	**Value (KS_statistics)**
model 4	13,48		*model 2*	-6677,7511	0,033599
p-value	**c-value**	**K-value**	**p-value**	**c-value**	**K-value**
p_1=1,45	c_1=1,5	k_1=598,9	p=1,45	c=1,553	k_1=621,1
p_2=1,56	c_2=2,045	k_2=245,3			k_2=2167,3

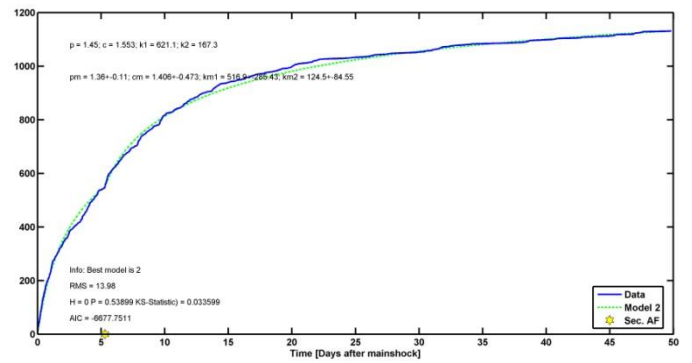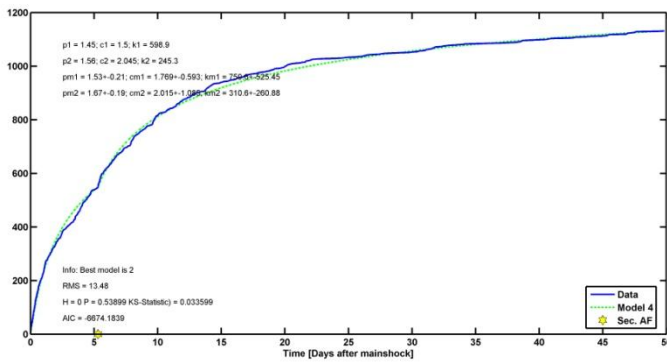**Table 11: Parameters derived from the modified Omori law.**

Figure 48,49: Number of aftershocks versus time (days after mainshock). The above two distributions result from the application of Omori law. More specifically, the left diagram shows the model 4 (best model RMS), while the corresponding model 2 (Best model (AIC-KS_statistics) is shown on the right. The estimated values for *p-value*, *c-value*, *k-value* are given in Table 11.

In line with the analysis of the previous aftershock sequences, for the earthquake of Mytilene, we study the distribution of the interevent times. The log–log plot of the CDF, $P(> T) = \frac{N(>T)}{N_0}$ of aftershocks interevent times has a typical Q-exponential pattern. According to the equations (8), (9) the value of *q* is *q=1.68* (same value as in the aftershock sequence of Zakynthos). The obtained value q ≈1.67 suggests a system with one degree of freedom.

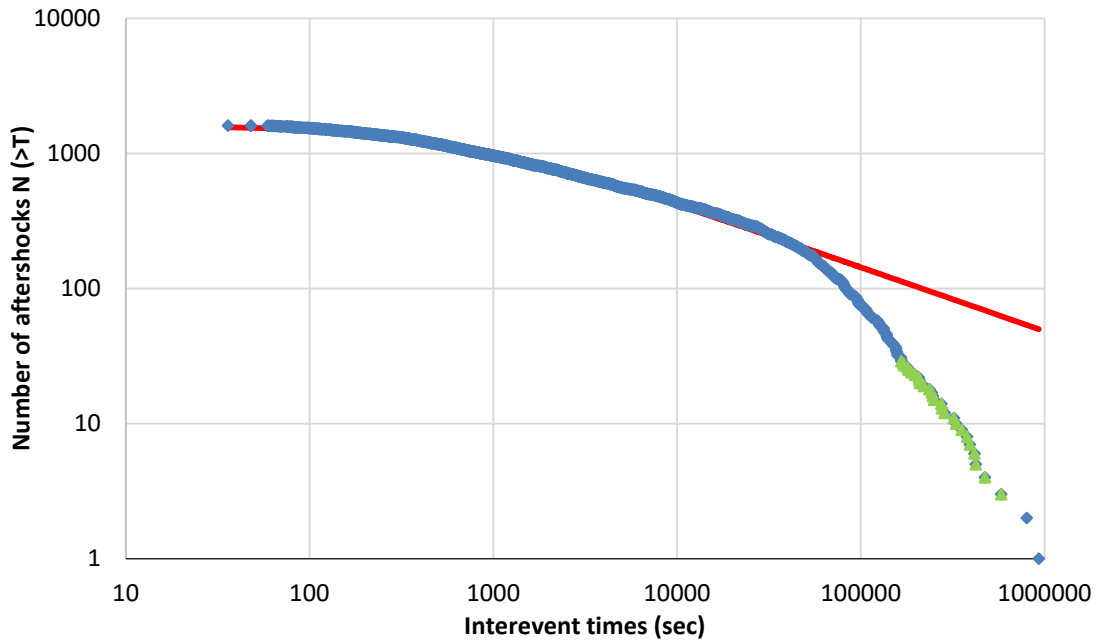**Figure 50: Interevent time distribution, $M>M_c$. The cumulative distribution functions of the interevent times for Mytilene earthquake. The red line is the q-exponential fitting with $q=1.68$.**

The diagram below shows the $\ln_Q P(>T)$ as a function of interevent time T for $q=1.68$. The transition from one system to another is close to $T_c \approx 42434$ s, based also on the correlation coefficient R^2.
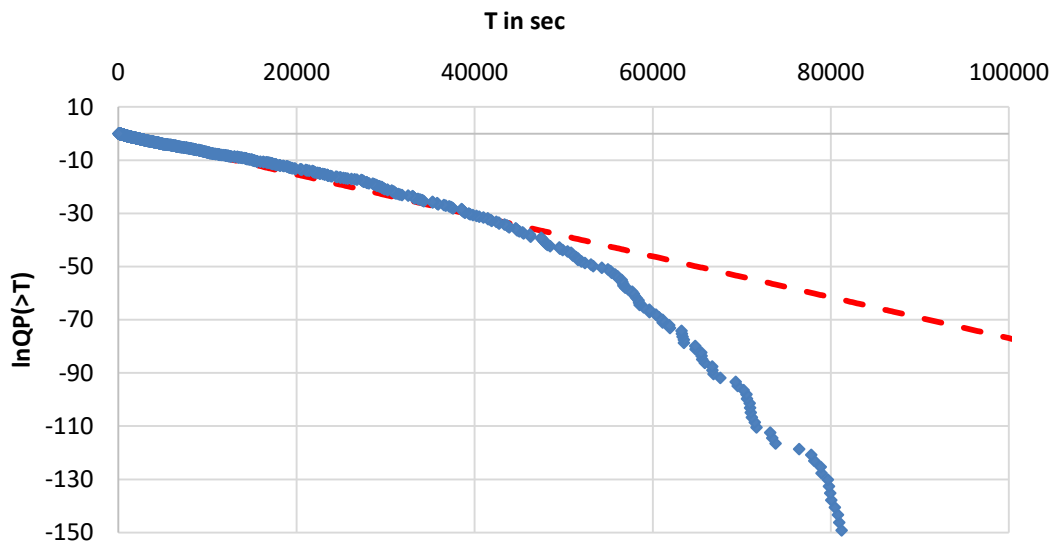

Figure 51: The Q-logarithmic function of the P (>T) as a function of the interevent times where the red line is the fitting with $q=1.68$. The deviation from the linearity suggests T_c values close to 42434 s.
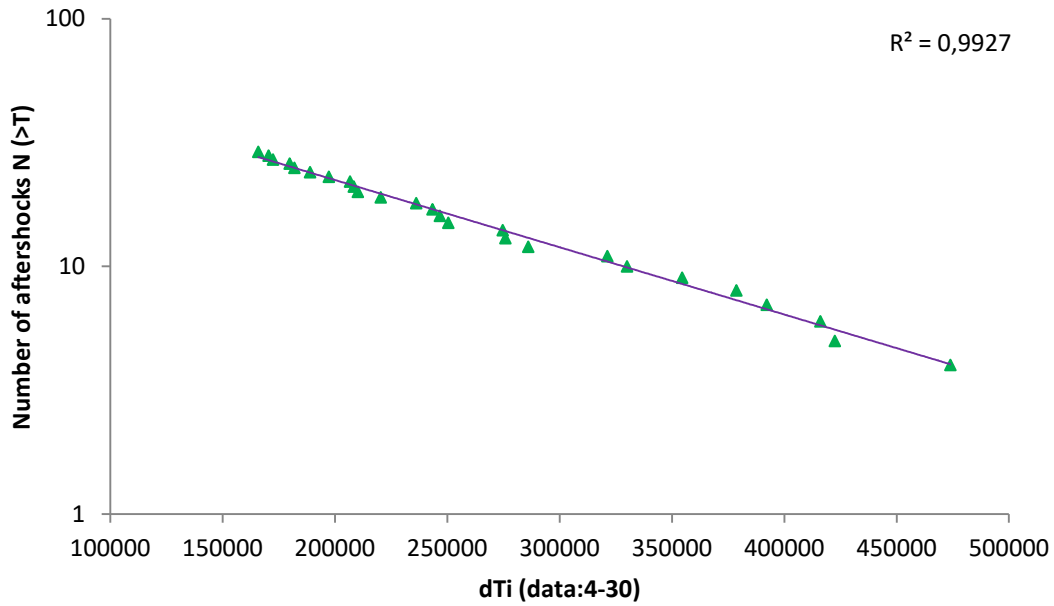
Figure 52: Diagram used to better estimate transition from one system to another. The results for the value of the T_c were based on the correlation coefficient, R^2. The data used to better calculate Tc are those shown with green triangles.

The evolution of interevent time T as a function of time from the main event (in seconds) has been moreover studied. The T_c value was marked as the red line (see table 6).
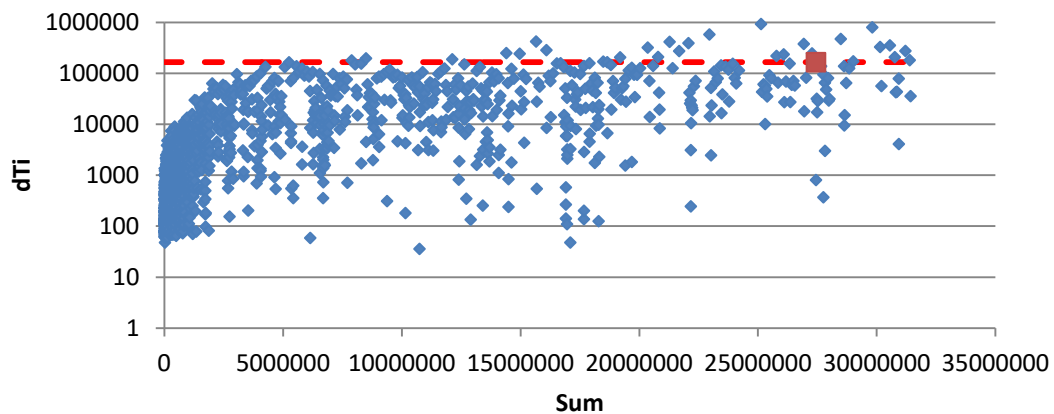

Figure 53: The evolution of interevent time T as a function of time t since the main event. The red line indicates the T_c value.

By plotting the aftershock magnitude as a function of logarithm of time t, second after the main event, we study the magnitude-time pattern in the first weeks of the aftershock sequence. The dashed line illustrates the short-term aftershock incompleteness effect (Vallianatos F., Pavlou K., 2021).
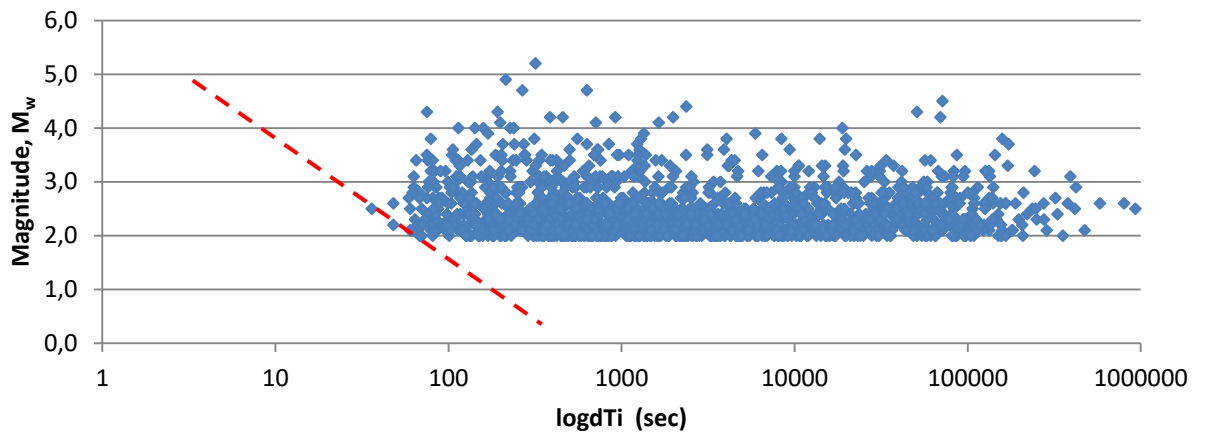
Figure 54: The magnitude-time pattern versus the logarithm of time.

The below parameters were taken out by Telesca's theory about the distribution of magnitude. The results of this distribution are represented in table 12. Figure 55 displays the log–linear plot which is characterized by a value *qMaq* equal to *qMag=1.54*.

Code qMagTelesca			
q$_{Mag}$	1,5354		
val	-33,0735		
ci	1,5181-1,5527	-581,5736	up to 515,4266

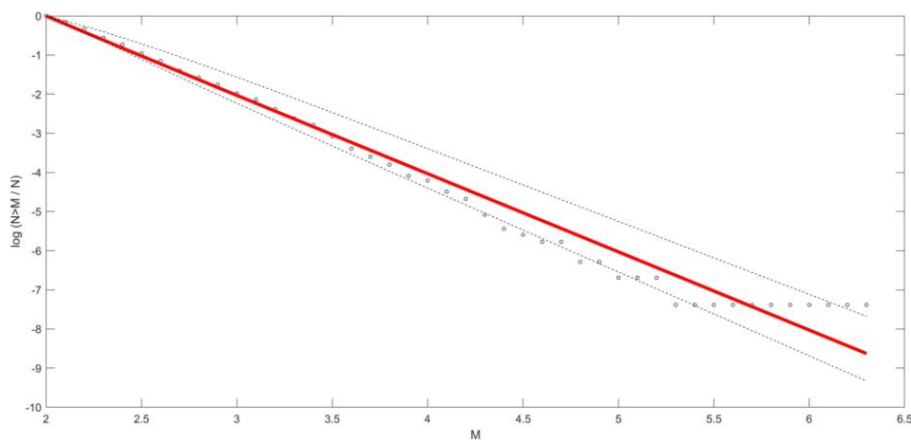**Table 12: parameters *qMag-value*, *ci-value*, *val-value*.**

Figure 55: Magnitude distribution, *M>M$_c$.* The earthquake cumulative magnitude distribution showed in this figure (ECMD). The red line is fitting with *qMag=1.54*.

Discussion

All earthquakes are followed by an aftershock sequence. Aftershocks occur in or near the fault of the main event, their temporal change follows the law of Omori and their sizes follow the law of Gutenberg Richter. The statistical properties of aftershock sequences are associated with three empirical scaling relations: (1) Gutenberg-Richter frequency-magnitude scaling, (2) the modified Omori's law for the temporal decay of aftershocks and last (3) the non-extensive statistical physics (NESP) by Tsallis entropy. It is essential to note that the validity of the G-R scaling is related to a fractal scaling between the number of earthquakes and their rupture areas. The modified Omori's law gives the temporal decay in the rate of aftershock occurrence. The above facts should be critically taken into account when dealing with aftershocks sequences. In this study, a detailed space-time-magnitude assessment on the aftershocks sequences over the last five years of strong earthquakes in Greece with magnitudes that reach up to M_w=7.0. We focused on the recent events, such as the M_w6.0 Elassona, the M_w5.1 Parnitha, the M_w6.6 Zakynthos, the M_L6.6 Kos and the M_w6.1 Mytilene earthquakes. By focusing on the analyses of aftershock parameters: *b-value* and *p-value* we come to the following conclusions: *b-value* change ranges from 0.73 to 1.04 and *p-value* ranges depending on which model it describes from 0.58 to 1.91. This relatively high or low *p-value* may be a result of the relatively fast or slow decay rate or the aftershock activity.

Moreover, the analysis of interevent times distribution of each aftershock sequence of each main shock, based on non-extensive statistical physics which is indicates a system in an anomalous equilibrium with a crossover from anomalous (*q>1*) to normal (*q=1*) statistical mechanics, as great interevent times approached. Thus, the obtained value *q ≈1.67* suggests a system with one degree of freedom. In all the cases of aftershock sequences that we have analyzed in this paper, we seem to be talking about systems characterized by a degree of freedom. However, there is a slight deviation in the *q* parameter for the Parnitha earthquake. It is also needed to clarify that this divergence, probability is due to the background seismicity. Furthermore, a scaling of the migration of aftershock zones as a function of the logarithm of time is discussed in terms of rate strengthening rheology that govern the evolution of the afterslip process.

In addition, we examined the distribution of magnitude based on Telesca's theory. Calculated *qMag* takes values from 1.53 to 1.56. Finally, it should be noted that the above results show that there is a correlation among aftershock parameters and an effective space-time-magnitude analysis of aftershock sequences is important.

Acknowledgements

References

V. Kapetanidis, A. Karakonstantis, P. Papadimitriou, K. Pavlou, I. Spingos, G. Kaviris, N. Voulgaris, (2020), The 19 July 2019 earthquake in Athens, Greece: A delayed major aftershock of the 1999 Mw = 6.0 event, or the activation of a different structure?, Journal of Geodynamics 139 (2020) 101766.

Bruce E. Shaw, Generalized Omori law for aftershocks and foreshocks from a simple dynamics, Institute for Theoretical Physics, University of California, Santa Barbara, CA 93106, Geophysical Research Letters, vol.20, no.10, pages 907-910, May 21,1993.

Vallianatos F., Pavlou K., (2020), Scaling properties of the Mw7.0 Samos (Greece), 2020 aftershock sequence.

Lekkas E. et al., (2021), The early March 2021 Thessaly earthquake sequence, Newsletter of Environmental, Disaster, and Crises Management Strategies, ISSN 2653-9454, Issue No.22 | March 2021.

Foumelis M., (2019), Velocity feld and crustal deformation of broader Athens plain (Greece) from a dense geodetic network, J. Appl. Geodesy 2019; 13(4): 305–316.

Tselentis G-A., Zahradnik J., The Athens Earthquake of 7 September 1999, Bulletin of the Seismological Society of America, 90, 5, pp. 1143–1160, October 2000.

Higgins M. D., (2009), Geology of the Greek Islands, ResearchGate, January 2009.

Diamantopoulou P., Voudouris K., (2008), Optimization of water resources management using SWOT analysis: The case of Zakynthos island, Ionian Sea, Greece, 2008.

Kati M., (1999), Deposit and diagenesis of Eocene formations of the Pre-Apulian Zone in Zakynthos island, Department of Geology, National University of Athens.

Zelilidis A., Kontopoulos N., Avramidis P., Piper D. J. W., (1998), Tectonic and sedimentological evolution of the Pliocene-Quatenary basins of Zakynthos island, Greece: case study of the transition from compressional to extensional tectonics, Basin Research (1998), 10, 393-408.

Lekkas E., Mavroulis S., (2018), The Mw 6.8 October 26, 2018 Zakynthos (Ionian Sea, Greece) Earthquake, Newsletter of Environmental, Disaster, and Crises Management Strategies, ISSN 2653-9454, Issue No. 10 | November 2018.

Kelepertsis A., Velitzelos E., (1992), Oligocene swamp sediments of Lesvos Island, Greece (geochemistry and mineralogy), ResearchGate, FACIES 27, 113-118.

Kalt A., Altherr R., Ludwig Th., (1998), Contact Metamorphism in Pelitic Rocks on the Island of Kos (Greece, Eastern Aegean Sea): a Test for the Na-in-Cordierite Thermometer, Journal of Petrology, Vol.39, no.4, pages 663-688.

Thomaidou E. L, (2009), The geological structure of Lesvos Island, Thessaloniki.

Geologic map of Lesvos Island (IGME; Hecht, 1974; Katsikatsos et al., 1982; Migiros, 1992; Soulakellis et al., 2006).

Stamatakis M., Drinia H., Taxeidis K., Tsourou Th., Dermitzakis M. D., Exploring Lesvos, University of Athens, Department of Geology, Natural History Collection of Vrissa.

Vallianatos F., Pavlou K., (2021), Scaling properties of the Mw7.0 Samos (Greece), 2020 aftershock sequence, Acta Geophysica: 69(18):18.

Tsallis C., (2009a), Introduction to non-extensive statistical mechanics: approaching a complex world, Springer, Berlin.

Tsallis C., (2009b), Nonadditive entropy and non-extensive statistical mechanics—An overview after 20 years. Braz J Phys 39:337–356.

Telesca L., (2012), Maximum likelihood estimation of the non-extensive parameters of the earthquake cumulative magnitude distribution. Bull Seismol. Soc Am 102:886–891

Vallianatos F., Michas G., Papadakis G., (2018), Non-extensive statistical seismology: an overview. In: Chelidze T., Vallianatos F., Telesca L. (eds), Complexity of seismic time series. Elsevier, Amsterdam, pp 25–60.

Rojas A.-R., Sigalotti L. Di G., Márquez E. L. F., Rendón O., (2019), Time Series Analysis in Seismology: Practical Applications, Elsevier Publications.

Abe, S., and N. Suzuki, (2003), Law for the distance between successive earthquakes, J. Geophys. Res., 108(B2), 2113, doi: 10.1029/2002JB002220, 2003.

Abe, S. and Suzuki N., (2005), Scale-free statistics of time interval between successive earthquakes, Physica A, 350, 588–596, 2005a.

Abe, S. and Suzuki N., (2005), Scale-invariant statistics of period in directed earthquake network, Eur. Phys. J. B, 44, 115–117, 2005b.

Shcherbakov R., Turcotte D. L., Rundle J.B., (2004), A generalized Omori's law for earthquake aftershock decay, GEOPHYSICAL RESEARCH LETTERS, VOL. 31, L11613, doi: 10.1029/2004GL019808, 2004.

Shcherbakov R., Turcotte D. L., Rundle J.B., Aftershock Statistics, (2005), Pure appl. Geophys, 162 (2005) 1051–1076, DOI 10.1007/s00024-004-2661-8, Birkhauser Verlag, Basel, 2005.

Papadimitriou P., Voulgaris N., Kassaras I., Kaviris G., Delibasis N., Makropoulos K., (2002), The Mw = 6.0, 7 September 1999 Athens Earthquake, Natural Hazards 27: 15–33, 2002.

Stavrakakis G. N., Chouliaras G., Panopoulou G., (2001), Seismic Source Parameters for the ML = 5.4 Athens Earthquake (7 September 1999) from a New Telemetric Broad Band Seismological Network in Greece, Natural Hazards 27: 47–60, 2002.

Caputo, R., Helly, B., Pavlides, S., Papadopoulos, G., (2004), Palaeoseismological investigation of the Tyrnavos Fault (Thessaly, Central Greece), Tectonophysics 394, 1–20., doi.org/10.1016/j.tecto.2004.07.047.

Chatzipetros, A., Lazos, I., Pavlides, S., Pikridas, C., Bitharis, S., (2018), Determination of the active tectonic regime of Thessaly, Greece: a geodetic data based approach. XXI International Congress of the CBGA, Salzburg, 227.

Wells, D.L. and Coppersmith, K.J., (1994), New empirical relationships among magnitude, rupture length, rupture width, rupture area, and surface displacement, Bulletin of the Seismological Society of America, 84, 974-1002.

Pavlides S., Chatzipetros A., Sboras S., Kremastas E., Chatziioannou A., (2021), The northern Thessaly strong earthquakes of March 3 and 4, 2021, and their neotectonic setting, Earthquake Geology Research Team, Thessaloniki, Greece, March 2021.

Wiemer S., Wyss M., (2000), Minimum magnitude of completeness in earthquake catalogs: Examples from Alaska, the western US and Japan, Bull Seism Soc Am 90:859–869.

Wyss M., Wiemer S., Zuniga R., (2001), Zmap: A tool for analyses of seismicity patterns, *typical applications and uses: a cookbook,* November, 2001.

Lekkas E., Voulgaris N., Karydis P., Tselentis G.-A., Skourtsos E., Antoniou V., Andreadakis E., Mavroudis S., Spirou N., Speis F., Papadimitriou P., Kouskouna V., Kassaras G., Kaviris G., Pavlou K., Sakkas V., Chouliaras G., (2017), PRELIMINARY REPORT, Lesvos Earthquake Mw 6.3, June 12,2017, Environmental, Disaster and Crisis Management Strategies.

Öztürk S., Şahin S., (2018), A statistical space-time-magnitude analysis on the aftershocks occurrence of the July 21th, 2017 MW = 6.5 Bodrum-Kos, Turkey, earthquake, Journal of Asian Earth Sciences, Elsevier, Journal of Geodynamics, Volume 172, 1 April 2019, Pages 443-457.

Ganas A., Briole P., Bozionelos G., Barberopoulou A., Elias P., Tsironi V., Valkaniotis S., Moshou A., Mintourakis I., (2020), The 25 October 2018 Mw = 6.7 Zakynthos earthquake (Ionian Sea, Greece): A low-angle fault model based on GNSS data, relocated seismicity, small tsunami and implications for the seismic hazard in the west Hellenic Arc, Elsevier, Journal of Geodynamics, Volume 137, June 2020, 101731.